NASA/TM–2014-218523

Direct Numerical Simulation of a Weakly Stratified Turbulent Wake

J. A. Redford
University of Southampton, Southampton, United Kingdom

T. S. Lund
NorthWest Research Associates, Inc., Boulder, Colorado

Gary N. Coleman
Langley Research Center, Hampton, Virginia

September 2014

NASA STI Program . . . in Profile

Since its founding, NASA has been dedicated to the advancement of aeronautics and space science. The NASA scientific and technical information (STI) program plays a key part in helping NASA maintain this important role.

The NASA STI program operates under the auspices of the Agency Chief Information Officer. It collects, organizes, provides for archiving, and disseminates NASA's STI. The NASA STI program provides access to the NASA Aeronautics and Space Database and its public interface, the NASA Technical Report Server, thus providing one of the largest collections of aeronautical and space science STI in the world. Results are published in both non-NASA channels and by NASA in the NASA STI Report Series, which includes the following report types:

- TECHNICAL PUBLICATION. Reports of completed research or a major significant phase of research that present the results of NASA Programs and include extensive data or theoretical analysis. Includes compilations of significant scientific and technical data and information deemed to be of continuing reference value. NASA counterpart of peer-reviewed formal professional papers, but having less stringent limitations on manuscript length and extent of graphic presentations.

- TECHNICAL MEMORANDUM. Scientific and technical findings that are preliminary or of specialized interest, e.g., quick release reports, working papers, and bibliographies that contain minimal annotation. Does not contain extensive analysis.

- CONTRACTOR REPORT. Scientific and technical findings by NASA-sponsored contractors and grantees.

- CONFERENCE PUBLICATION. Collected papers from scientific and technical conferences, symposia, seminars, or other meetings sponsored or co-sponsored by NASA.

- SPECIAL PUBLICATION. Scientific, technical, or historical information from NASA programs, projects, and missions, often concerned with subjects having substantial public interest.

- TECHNICAL TRANSLATION. English-language translations of foreign scientific and technical material pertinent to NASA's mission.

Specialized services also include organizing and publishing research results, distributing specialized research announcements and feeds, providing information desk and personal search support, and enabling data exchange services.

For more information about the NASA STI program, see the following:

- Access the NASA STI program home page at *http://www.sti.nasa.gov*

- E-mail your question to help@sti.nasa.gov

- Fax your question to the NASA STI Information Desk at 443-757-5803

- Phone the NASA STI Information Desk at 443-757-5802

- Write to:
  STI Information Desk
  NASA Center for AeroSpace Information
  7115 Standard Drive
  Hanover, MD 21076-1320

NASA/TM–2014-218523

Direct Numerical Simulation of Weakly Stratified Turbulent Wake

J. A. Redford
University of Southampton, Southampton, United Kingdom

T. S. Lund
NorthWest Research Associates, Inc., Boulder, Colorado

Gary N. Coleman
Langley Research Center, Hampton, Virginia

National Aeronautics and
Space Administration

Langley Research Center
Hampton, Virginia 23681-2199

September 2014

Acknowledgments

This project was supported by the Revolutionary Computational Aerosciences project under NASA's Fundamental Aerodynamics program, by the UK Ministry of Defence (Dstl project RD027-02854, managed by Dr R.P.Hornby) and by the UK Turbulence Consortium, funded by the UK Engineering and Physical Sciences Research Council (EPSRC), under Grants EP/D044073/1 and EP/G069581/1. It made use of the facilities of HPCx and HECToR, the UK's national high-performance computing service, which is provided by UoE HPCx Ltd at the University of Edinburgh, Cray Inc and NAG Ltd, and funded by the Office of Science and Technology through EPSRC's High End Computing Programme. We are grateful to Dr. S. L.Woodruff for reviewing the manuscript.

Available from:

NASA Center for AeroSpace Information
7115 Standard Drive
Hanover, MD 21076-1320
443-757-5802

Abstract

Direct numerical simulation (DNS) is used to investigate a time-dependent turbulent wake evolving in a stably stratified background. A large initial Froude number is chosen to allow the wake to become fully turbulent and axisymmetric before stratification affects the spreading rate of the mean defect. The uncertainty introduced by the finite sample size associated with gathering statistics from a simulation of a time-dependent flow is reduced, compared to earlier simulations of this flow. The DNS reveals the buoyancy-induced changes to the turbulence structure, as well as to the mean-defect history and the terms in the mean-momentum and turbulence-kinetic-energy budgets, that characterize the various states of this flow – namely the three-dimensional (essentially unstratified), non-equilibrium (or 'wake-collapse') and quasi-two-dimensional (or 'two-component') regimes observed elsewhere for wakes embedded in both weakly and strongly stratified backgrounds. The wake-collapse regime is not accompanied by transfer (or 'reconversion') of the potential energy of the turbulence to the kinetic energy of the turbulence, implying that this is not an essential feature of stratified-wake dynamics. The dependence upon Reynolds number of the duration of the wake-collapse period is demonstrated, and the effect of the details of the initial/near-field conditions of the wake on its subsequent development is examined.

1 Background and objectives

This study is concerned with the effects of stable buoyancy upon the evolution of a turbulent wake. These effects can be parameterized by the Froude number $F = U/NL$, where U and L are relevant velocity and length scales and $N = [-g(\mathrm{d}\overline{\rho}/\mathrm{d}z)/\rho_\infty]^{1/2}$ is the Brunt-Väisälä frequency (where g is the gravitational acceleration, z is the vertical coordinate, $\overline{\rho}$ is the mean background density and ρ_∞ is a characteristic/reference density). The Froude number is an inverse measure, being small when buoyancy is important and large when it is not. For the flow over a wake-generating body, an appropriate Froude number can be defined as $F_\infty = 2U_\infty/ND$, where U_∞ and D are the speed and effective cross-sectional diameter of the wake-generating body. A local, time-dependent, alternative is the deficit Froude number, $F_d = 2U_d/N\delta$, where U_d and δ are the maximum mean wake-velocity deficit and mean wake width. Since the velocity deficit decreases with distance from the body while the wake width increases, the wake Froude number strictly decreases with distance. This implies all wakes in stratified fluids will be affected by buoyancy at some point in their development.

Here we consider the weakly stratified case with initially high Froude number ($F_d \gg 1$), such that the wake is largely unaffected by buoyancy for some distance downstream of the body. Weakly stratified wakes evolve through three distinct regimes, which Spedding [1] referred to as the three-dimensional (3D), non-equilibrium and quasi-two-dimensional states. A review of the towed-wake experiments from which this picture derives is given by Diamessis, Spedding & Domaradzki [2], while a model that recovers the three regimes, along with two others, is presented by Meunier, Diamessis & Spedding [3].

During the 3D regime the high-F_∞ wake is initially unaffected by buoyancy and thus produces fully three-dimensional turbulent motions for a period of time, while the wake-defect Froude number remains greater than order 1. The mean and turbulence statistics are consistent with unstratified flows during this time and exhibit self-similar behavior indistinguishable from that observed in unstratified wakes (Tennekes & Lumley [4], Bevilaqu & Lykoudis [5]). This situation is in contrast to flows with initial F_d of order one or smaller, which are immediately altered by stratification, so that the canonical self-similar state is never realized. In the extreme initial-$F_d \to 0$ case, buoyancy suppresses vertical motion to the extent that three-dimensional turbulence never appears (Chomaz *et al.* [6], Riley & Lelong [7]). For towed-sphere experiments, the critical value below which the 3D regime

does not exist is $F_\infty \approx 4$; cf. Dommermuth *et al.*, [8].

When the initially three-dimensional turbulence in the high-F_∞ wake begins to 'feel' the effects of buoyancy, the non-equilibrium (NEQ) (also known as 'vertical collapse') regime begins. (The term 'non-equilibrium' can be viewed as a synonym for 'intermediate' or 'transitional', and should not be interpreted literally: it does not imply, for example, that in the pre-NEQ state the rates of production and dissipation of turbulence kinetic energy balance, since this type of equilibrium does not happen even in the purely unstratified self-similar benchmark.) When the wake enters the NEQ phase, it ceases to spread vertically; in fact, the height has been observed in some cases to slowly decrease with time during this period (Brucker & Sarkar [9]; Diamessis *et al.* [2]; Lin & Pao [10], the latter for the self-propelled case), although this may be at least in part a consequence of how the height is defined. As we will see below, a distinction should be made between the heights based on the mean defect (typically measured using a Gaussian curve fit) and on the extent of the wake turbulence (revealed for example by shadowgraph or dye visualizations).

As the wake stops spreading vertically, its lateral growth continues at roughly the same rate observed during the 3D phase (Diamessis *et al.* [2]). (We reserve the term 'lateral' to indicate the direction aligned with the axis orthogonal to the streamwise-vertical plane.) Whether the rate of lateral spreading remains exactly or only approximately constant as the flow passes from the 3D to NEQ states is an open question. Brucker & Sarkar [9] cite different power-law exponents for the mean-defect width during the different regimes, while Diamessis *et al.* [2] find $t^{1/3}$ behavior for the entire wake history.

The NEQ period is also characterized by a large reduction in the rate of decay $|\mathrm{d}U_d/\mathrm{d}t|$ of the maximum mean defect velocity U_d, and also the rate of decay of the turbulence kinetic energy. Spedding [1] and others (e.g. Dommermuth *et al.* [8]; Diamessis *et al.* [2]) have described these as 're-stratification' effects, attributed to the transfer of potential to kinetic energy, as the wake turbulence collapses, and heavy/cold fluid parcels fall, and light/warm ones rise, towards their original positions. Although this explanation is plausible and consistent with the behavior of the mean defect, it is not the only possibility, since the mean and turbulence kinetic energy can also be enhanced by alterations to the production and dissipation processes (cf. Brucker & Sarkar [9]). We shall present evidence for a picture of NEQ dynamics that is not based on the net transfer of potential to kinetic energy, which for the turbulence is consistently in the opposite direction and for the mean does not act directly upon the streamwise component.

The NEQ phase is observed to begin at roughly two buoyancy periods ($Nt \approx 2$) for a wide range of $F_\infty > 4$ (Spedding [1]). Its duration, on the other hand, has been predicted by Meunier *et al.* [3], and demonstrated by the DNS of Brucker & Sarkar [9] and the large-eddy simulations (LES) of Diamessis *et al.* [2], to increase with Reynolds number $R_\infty = U_\infty D/\nu$. While the evidence for this Reynolds-number dependence is strong, it remains at present rather qualitative, since it is influenced by the statistical uncertainty associated with finite-domain numerical simulations (see below).

After the NEQ phase, the wake enters the quasi-two-dimensional (Q2D) state, characterized by the emergence of large-scale coherent structures. (Godeford & Cambon [11] point out that 'quasi-two-component' is a more accurate description of flows like this, whose vertical motions have been strongly attenuated by stable buoyancy, since significant vertical variations of the other two components are not necessarily negligible. Nevertheless, to be consistent with previous studies, we shall continue to use 'Q2D' to refer to this aspect of the wake evolution.) The towed-sphere measurements of Chomaz *et al.* [6] revealed that flattened 'pancake-like' eddies eventually appear for both weak and strong stratification (cf. Spedding [12]). The maximum mean velocity begins to decrease more quickly than it did during the NEQ regime, while the mean defect spreads laterally at a rate comparable to the 3D value. The vertical spreading also begins again, growing at a rate consistent with viscous diffusion (Meunier *et al.* [3], Brucker & Sarkar [9], Diamessis *et al.* [2]).

While the effects of buoyancy that lead from the 3D to the NEQ and then the Q2D regimes are well-understood on a qualitative level, there is lesser understanding of the detailed turbulent processes that drive the regime changes. Our aim in the present study is to use numerical simulation to quantify the mechanisms involved, and thereby provide answers to questions such as the one mentioned above regarding the hypothesized transfer of potential to kinetic energy during the NEQ regime. Nearly all wake simulations performed to date have made use of the temporal idealization where a fixed streamwise segment of the wake is evolved in a reference frame attached to the undisturbed fluid. The weak streamwise variation of statistics is ignored so that periodic boundary conditions can be used in the streamwise direction. This configuration allows for very efficient numerical procedures and has proven to yield results that are in reasonable agreement with laboratory measurements (cf. Gourlay *et al.* [13]). Although we employ the same temporal idealization as those before us, we have chosen a longer streamwise domain than has been used in prior studies. Since the streamwise direction is assumed to be homogeneous, it forms the basis for computing the (time-dependent) turbulence statistics. While relatively short domains require fewer mesh points and proportionally less computer time, they provide a smaller averaging base at each time; a domain of minimal size may contain only one or two of the large-scale turbulent structures present at that instant in time. While such a simulation progresses without difficulty, there can be large uncertainty, which increased in time, in the computed statistics due to inadequate sample. Here we use a streamwise domain size that is between 1.2 and 5.6 times longer than those employed in previous wake simulations (cf. Gourlay *et al.* [13], Brucker & Sarkar [9], and Diamessis *et al.* [2]). This extended streamwise domain allows for a greater population of 'large-eddy samples' and provides less uncertain statistics. This strategy leads to resolution of earlier discrepancies, such as that in the lateral spreading rate during the NEQ regime reported by [9] and [2].

As with the discrepancy in the lateral wake spreading rate, there is no consensus on the Reynolds-number dependence of the duration of the NEQ regime. This feature is also influenced by statistical uncertainty, and prior results reported by Brucker & Sarkar [9] and Diamessis *et al.* [2] have relatively high uncertainty due to limited large-eddy samples. The increased domain size and a separate numerical experiment (discussed in detail below) will be used to demonstrate the factors affecting the time at which the NEQ state begins to transition to the Q2D regime.

Finally, the initial-condition dependence of the wake development will be examined, in light of the non-universality of the self-similar states observed for late axisymmetric wakes in unstratified media. The non-universality of the unstratified case is exemplified by mean spreading rates and turbulence-to-mean ratios that vary with the shape of the wake-creating object (Bevilaqua & Lykoudis [5]) (although they *eventually*, at distances corresponding to 1000s of body sizes downstream, relax to a universal value; see Redford *et al.* [14], referred to hereinafter as RCC). This non-universality has been traced to differences in the near-field turbulence structures shed from bodies of different shape. For the stratified counterpart, the available data suggest that the structures of the early and late wake are unrelated, with pancake eddies ultimately resulting from a wide variety of initial states, some of which are non-turbulent or even non-wake-like [2,13,15,16]. Furthermore, Spedding [1] showed that for sphere wakes, nominal universality is obtained for the mean-defect history $U_d(t)/V_\infty$ when weighted by $F_\infty^{2/3}$. This scaling was generalized to bodies of various shapes by Meunier & Spedding [17] (see also [3]) by accounting, via an effective diameter, for the net momentum extracted by the body. The founding assumption of their model will be assessed below.

The issues raised above will be addressed using DNS of a wake at high F_∞ and relatively high R_∞. To put this simulation in context, we mention the earlier numerical studies of stably stratified wakes generated by constant-velocity axisymmetric towed bodies performed, for high-F_∞, by Gourlay *et al.* [13] (via DNS), Diamessis *et al.* [2] (LES) and

Brucker & Sarkar [9] (DNS), the latter as part of a study of differences between wakes downstream of towed- and self-propelled bodies in high- and low-F_∞ backgrounds (de Stadler & Sarkar's [18] DNS includes the effect of body acceleration for moderate stratification). Lower F_∞ cases have been simulated by Dommermuth *et al.* [8], by LES, and (for a range of Prandtl numbers) de Stadler *et al.* [19], by DNS. Provided it can reach relevant Reynolds numbers (and produce accurate statistics), a numerical approach has many advantages, supplying detail not available from experiment. For example, Gourlay *et al.*'s , [13] DNS revealed the vortex-ring structure underlying the Q2D pancake eddies, while the LES of Diamessis *et al.* [2] documented the presence of small-scale Kelvin-Helmholtz instabilities during the NEQ regime and its Reynolds-number dependence. Dommermuth *et al.*'s [8] low-F_∞ LES quantified the relative importance of the terms in the mean- and turbulence-kinetic-energy budgets, during the NEQ and Q2D regimes, that ensue when the turbulence is immediately affected by buoyancy. Similar exercises were performed by Brucker & Sarkar [9] and deStadler & Sarkar [18] for their towed- and self-propelled-body flows.

To summarize, we will use DNS to:

1. Obtain results with improved 'eddy sample size' (via increased streamwise domain length), to reduce the uncertainty of the statistics, especially the mean wake spreading rate.

2. Assess more completely how the effects of buoyancy alter the wake's mean momentum and turbulence energy budgets.

3. Determine whether or not there is a net transfer of potential to kinetic energy during the wake collapse in the NEQ regime.

4. Quantify the Reynolds-number dependence of the duration of the NEQ regime.

5. Demonstrate how the wake development is affected by the details of the initial condition used in the numerical simulation, comparing with earlier simulation results to explore the extent to which mean-defect histories exhibit universality.

In § 2, the numerical approach, initialization strategy, and DNS parameters are described. Section 3 documents the wake development in terms of flow visualisations, mean-flow statistics, and the budgets of mean momentum, and mean and turbulence kinetic energy. Closing comments and conclusions are summarized in § 4.

2 Problem formulation, numerical strategy and parameters

Following Gourlay *et al.* [13] (cf. [2,8,9,18,19]), we (as in RCC) invoke a Galilean transformation, and emulate the actual, spatially developing wake with a parallel-flow, temporally developing idealization. The resulting streamwise homogeneity allows efficient DNS with a standard triply periodic FFT-based pseudo-spectral method [20].

For the high-Froude-number flow studied here, vertical density variations are negligible compared to the background reference density ρ_∞, allowing stable stratification to be accounted for with the Boussinesq (divergence-free velocity) approximation. Molecular diffusion of the (temperature-dependent) density field is matched to that for the velocity field by assuming the Prandtl number $\nu/\alpha = 1$ (cf. [19]), where ν is the kinematic viscosity and α is the thermal diffusivity, both of which are assumed constant in space and time (and therefore independent of temperature). The pressure variable in the incompressible Navier-Stokes equations is eliminated using a velocity-vorticity formulation [21]. A low-storage

third-order temporal discretization [22] is applied to the nonlinear terms, while the viscous terms are treated analytically [23].

The coordinate $x = x_1$ denotes the streamwise/longitudinal direction, along the wake axis, with $u = u_1$ the corresponding streamwise velocity, defined such that positive values point 'upstream' and the maximum occurs at the centerline (figure 9). Because of the parallel-flow assumption, the uniform background/freestream velocity V_∞ amounts to an arbitrary Galilean shift; we chose $V_\infty = 0$, which implies $u \to 0$ far from the wake centerline. The lateral ('spanwise') and vertical directions are respectively $y = x_2$ and $z = x_3$ (positive upwards), with velocities $v = u_2$ and $w = u_3$, such that x-y planes are normal to the gravity vector $g_i = -g\delta_{i3}$.

Before discussing the numerical parameters, we describe the three types of averaging used in this paper. The Reynolds decomposition is defined with respect to the mean (denoted by an overbar) formed by averaging over the homogeneous streamwise direction x; this mean thus varies with lateral and vertical position, and time: e.g. $\overline{u} = \overline{u}(y, z, t)$. (Note that, unlike for the unstratified wake simulated in RCC, averaging over the azimuthal direction is not appropriate.) A prime ($'$) indicates a deviation from this mean, such that the Reynolds stresses, density-fluctuation variance and turbulent buoyancy flux are written respectively as $-\overline{u_i' u_j'}$, $\overline{\rho'\rho'}$ and $-\overline{\rho' w'}$. As in Spedding [1], we also examine histories of bulk averages of Reynolds-averaged quantities, taken across the inhomogeneous directions (y and z) of the mean defect, over the region where $\overline{u} > 0.05\,U_d$ (Spedding's mean was over horizontal and vertical planes where $\overline{u} > 0.2\,U_d$). These averages are indicated with angle brackets: $\langle k \rangle = (1/2)\langle \overline{u_i' u_i'} \rangle = (1/2)\int_0^{\Lambda_z}\int_0^{\Lambda_y} \psi\, \overline{u_i' u_i'}\,\mathrm{d}y\,\mathrm{d}z/\Psi$, where $\psi = \psi(y,z)|_{\overline{u}/U_d > 0.05}$ is unity if $\overline{u}(y,z) > 0.05\,U_d$ and zero otherwise, and $\Psi = \int_0^{\Lambda_z}\int_0^{\Lambda_y} \psi\,\mathrm{d}y\,\mathrm{d}z$. A third type of statistic (indicated by braces $\{\ \}$) is formed from cross-wake integration (not averaging) over the entire y-z domain, of Reynolds-averaged quantities; examples include the total/integrated turbulence kinetic energy (TKE) $\{k\} = (1/2)\int_0^{\Lambda_z}\int_0^{\Lambda_z} \overline{u_i' u_i'}\,\mathrm{d}y\,\mathrm{d}z$ and its rate of production $\{\mathcal{P}_{\mathsf{tke}}\} = -\int_0^{\Lambda_z}\int_0^{\Lambda_z} (\overline{u_i' u_j'}\partial\,\overline{u}_i/\partial x_j)\,\mathrm{d}y\,\mathrm{d}z$.

Based on our earlier experiences with DNS of unstratified turbulent wakes (RCC), the wake is initialised as a sequence of vortex rings, identical to Case VR of RCC apart from the ring spacing (see their figure 1a), embedded in a stably stratified background with imposed constant/uniform mean-density gradient $\Gamma = (\mathrm{d}\rho/\mathrm{d}z)_\infty < 0$. This strategy was found to be an efficient way to produce fully developed wake turbulence containing mature turbulent structures, which – while not necessarily corresponding to those generated by a realistic wake-creating body in a real-world application – allows us to perform a numerical experiment that can be used to address the issues raised above (such as the effect of the details of the initial conditions on late-wake development).

In order to simulate the wake using periodic boundary conditions, the transported density variable ($= \overline{\rho}(z,t) + \rho'(x,y,z,t)$) is defined as the perturbation from the background density field $\rho_\infty + z\Gamma$ (where the origin of the z-axis is, say, in the center of the computational domain).

As in Shariff [24], each ring in the sequence is represented as a circular loop, of radius r_0 in y-z planes, of Gaussian azimuthal core vorticity ω_θ, with $\omega_\theta = (\gamma/\pi\delta_\omega^2)\exp\left[-(s/\delta_\omega)^2\right]$, where γ is the ring's circulation, $s^2 = (x-x_0)^2 + (r-r_0)^2$, $r^2 = (y-y_0)^2 + (z-z_0)^2$ and (x_0, y_0, z_0) is the location of the centre of the ring in question. The length-scale δ_ω defines the thickness of the vortex core (chosen as $\delta_\omega = 0.4r_0$). The rings are spaced uniformly every $2\pi r_0/3$ along the wake axis (x, y_0, z_0) (RCC used $16\pi r_0/27 \approx 0.59\pi r_0$); the rings combine to induce an initial mean velocity defect of maximum velocity U_{do} and width h_o, the latter defined as the radial distance from the wake centreline to the location at which the mean streamwise velocity $\overline{u}$ is half of U_d.

The wake turbulence is the result of a nonlinear/bypass transition, which is triggered by a $\Delta r = \pm 0.004 r_0$ maximum radial displacement of the ring circumference, in the y-z

plane, for each of the azimuthal modes $5-32$, with random azimuthal phases, using different random-number seeds for each ring. As the individual vortex rings break down and disturb their neighbours, a vericose-type instability ensues (see figure 5*a* of RCC), leading to fully developed turbulence relatively quickly – much sooner than, for example, when very-small-amplitude disturbances are added to a mean defect profile, such that transition is via growth of the helical linear-instability modes (as was done for Case SD of RCC). The approach used by Gourlay *et al.* [13] also avoids the need to simulate the natural linear-instability transition process, by prescribing a Gaussian mean velocity and superimposing random finite-amplitude perturbations whose magnitudes were set by matching a desired energy spectrum, and then clipped/filtered in physical space with an axisymmetric/cylindrical window. Similar procedures were followed by Brucker & Sarkar [9] and Diamessis *et al.* [2], although the former's DNS involved an initial adjustment period during which the mean flow was held fixed as the fluctuations developed, and the latter's LES required a precursor 'relaxation' simulation, during which the effective gravity was slowly increased. Despite being necessarily somewhat 'synthetic' in nature, those initialization schemes all produced statistics that very quickly exhibit expected behavior (see figure 21). The primary difference between the present and earlier strategies is that here coherent structures are 'hard wired' into the initial-condition turbulence.

The initial Froude number specified here is quite large, to ensure the wake turbulence is fully developed and physical when it is first affected by the stratification. The initial mean-defect Froude number $F_{do} = U_{do}/Nh_o = 23.7$; this corresponds to $F_\infty = 2V_\infty/ND$ of approximately 130, assuming the uniform flow speed $V_\infty \approx 5U_{do}$ and virtual-body diameter $D \approx 2h_o$ (see RCC). The initial mean-defect Reynolds number $R_{do} = U_{do}h_o/\nu = 2625$, such that the equivalent $R_\infty = V_\infty D/\nu \approx 2.6 \times 10^4$. This is well above the critical value of $R_\infty \approx 5 \times 10^3$, found by Spedding, Browand & Fincham [25] to be required for the turbulent wake structures and decay rates to exhibit self similarity – although it is not above the threshold (if one exists) beyond which all features (such as the duration of the various self-similar regimes) can be expected to be independent of Reynolds number (cf. Diamessis *et al.* [2]).

A modified version of this case will also be considered, which is equivalent except that beginning from $Nt = 1.9$ the viscosity varies at each time step, such that the mean-defect Reynolds number, based on the integral scale $r^* = ((\ln 2/\pi)(I_d/U_d))^{1/2}$, where $I_d = \{\overline{u}\}$ is the volume-flux deficit, remains fixed thereafter at $U_d\, r^*/\nu = 1500$; see + symbol in figure 1*c*, *d*. (The regridding/domain-expansion strategy described below was also employed, although, towards the end of the run, not at identical times.) Results from this 'artificial' numerical experiment (cf. [26]), which we shall refer to as Case R1500, will be compared to those from the primary (constant-viscosity/variable-Renolds-number) DNS, to determine the Reynolds-number dependence of the mean-defect histories; unless otherwise stated (see figure 7) all the new simulation results shown below will be from the primary DNS. Two additional test runs were also performed, to explore numerical-validation issues, as explained below.

For Gourlay *et al.* [13], $F_{do} = 34.0$ and $R_{do} = 1472$. The more recent simulations tended to use lower F and higher R: Brucker & Sarkar's [9] Case TR50F04 (i.e. $F_\infty/2 = V_\infty/ND = 4$, $R_\infty = 50\,000$) corresponds to $F_{do} \approx 0.75$ and $R_{do} \approx 3250$ (they assume $U_{do}/V_\infty = 0.11$ and $D \approx 1.7h_o$). They also simulated a lower-R, higher-F flow with which we will compare (their 'TR10F20'), with $(F_{do}, R_{do}) \approx (3.75, 650)$. Comparison will also be made with the recent $F_\infty = 64$ ($F_{do} \approx 14.5$), $R_\infty = 10^5$ ($R_{do} \approx 1.1 \times 10^4$) LES of Diamessis *et al.* [2], for which the eddy-resolving capability was comparable to the present DNS. In fact, although the smallest resolved scales are not those that actually appear at $R_\infty = 10^5$, the LES has the advantage of taking full benefit of the available spatial resolution – since the magnitude of the subgrid-scale viscosity of the LES can be smaller than the molecular viscosity of the DNS – and thus has the capacity to capture scales smaller than those of an over-resolved

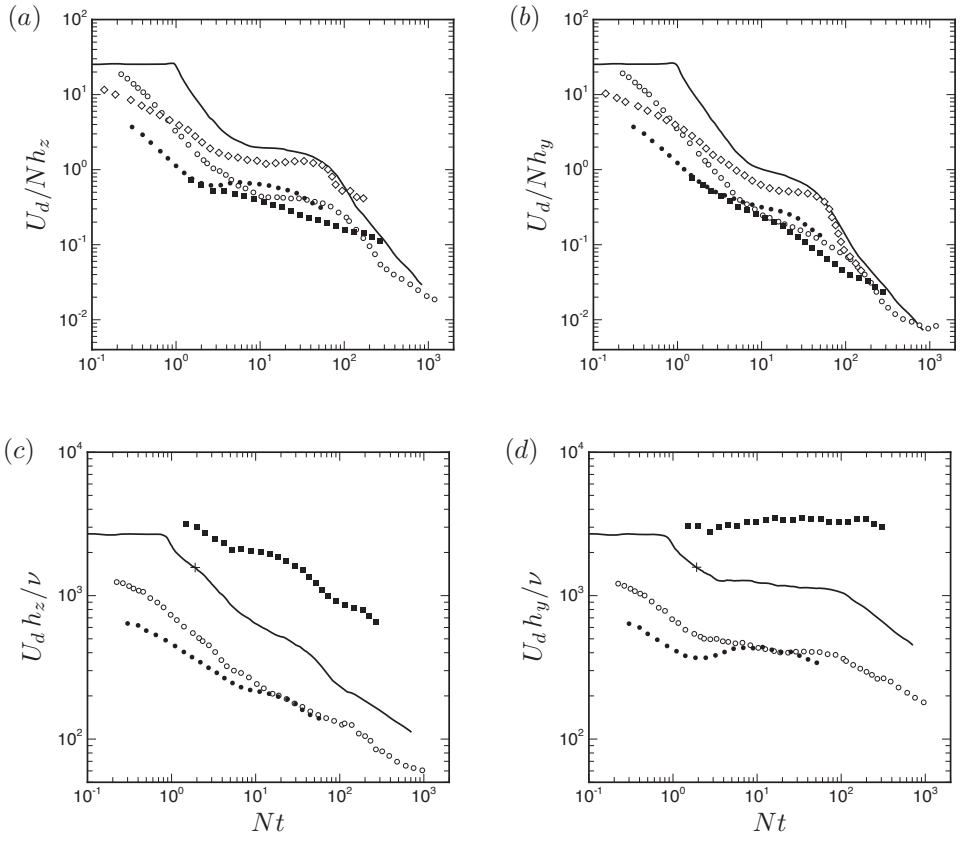

Figure 1. Mean (a, b) Froude number $F_d = U_d/Nh$ and (c, d) Reynolds number $R_d = U_d h/\nu$ histories: ———, present DNS $[(F_{do}, R_{do}) = (23.7, 2223)]$; +, time at which the variable-viscosity run (Case R1500) first reaches its minimum Reynolds number, $U_d\, r^*/\nu = 1500$ (see discussion regarding figure 7); ∘, Gourlay *et al.* [13] $[(F_{do}, R_{do}) \approx (34, 1472)]$; ■, Case TR50F04 of Brucker & Sarkar [9] $[(F_{do}, R_{do}) \approx (0.75, 3250)]$; •, Case TR10F20 of Brucker & Sarkar [9] $[(F_{do}, R_{do}) \approx (3.75, 650)]$; ⋄, Case R100F64 LES of Diamessis *et al.* [2] $[(F_{do}, R_{do}) \approx (14.5, 11\,000)]$.

DNS at smaller Reynolds number, such as is used here.

The variations of the mean-defect-based Froude and Reynolds numbers for the present and earlier simulations are shown in figure 1, defined in terms of both the wake's mean height h_z and width h_y. Evidence of each of the 3D, NEQ and Q2D regimes can be seen. The tendency for the Froude numbers to all fall monotonically indicates that all the flows, even those with very large F_{do}, eventually are dominated by buoyancy effects. The anisotropy introduced by the stable stratification can be inferred in the differences between the Froude and Reynolds numbers based on h_z and h_y. The wake evolution is such that the power-law decay of the height-based Reynolds number $U_d\, h_z/\nu$ varies little over the life of the flow, while $U_d\, h_y/\nu$ remains relatively constant, especially during the NEQ phase (cf. Diamessis *et al.* [2]). The time required ($t \approx 1/N$) for the vortex-ring initialization (solid line) to produce a fully turbulent state is apparent, which can be contrasted with the approaches used to define the $Nt = 0$ state for the other simulations (recall that all involved specifying finite disturbances typical of the fully developed wake downstream of a sphere). The question of appropriate virtual origins, needed when comparing the present and earlier cases, will be taken up below.

To prepare for the possibility of the wake generating significant internal/buoyancy waves, a 'fringe' region is adopted at the lateral and vertical edges of the periodic domain, to prevent the energy radiated in the waves from re-entering the domain, and spuriously affecting the wake dynamics. A forcing term $\mathbf{F}$ (similar to that used by de Stadler *et al.* [19] and de Stadler & Sarkar [18]) is added to the right-hand-side $\mathbf{R}$ of the momentum and scalar equations

$$\frac{\partial \mathbf{q}}{\partial t} = \mathbf{R} + \mathbf{F}, \tag{1}$$

which, in the fringe zone, drives $\mathbf{q} = (u, v, w, \rho')^T$ to a mean reference $\hat{\mathbf{q}}$, defined as its average along the edge of the domain. The fringe forcing is written as $\mathbf{F} = -\sigma(y,z)(\mathbf{q} - \hat{\mathbf{q}})$ where the fringe function

$$\sigma(y,z) = C_\sigma \left[\, \sigma_y(y) + \sigma_z(z) - \sigma_y(y)\sigma_z(z) \right], \tag{2}$$

for $0 \le y \le \Lambda_y$ and $0 \le z \le \Lambda_z$, with $C_\sigma = 0.04$ and

$$\sigma_y(y) = 1 - \frac{1}{2}\left\{ \tanh\left[a_f \left(\frac{2y}{\lambda_y} - 1 \right) \right] + \tanh\left[a_f \left(\frac{2(\Lambda_y - y)}{\lambda_y} - 1 \right) \right] \right\}, \tag{3}$$

$$\sigma_z(z) = 1 - \frac{1}{2}\left\{ \tanh\left[a_f \left(\frac{2z}{\lambda_z} - 1 \right) \right] + \tanh\left[a_f \left(\frac{2(\Lambda_z - z)}{\lambda_z} - 1 \right) \right] \right\}, \tag{4}$$

where $a_f = 2.5$, $\lambda_y = 30\Lambda_y/N_y$, $\lambda_z = 30\Lambda_z/N_z$ and Λ_y and Λ_z are respectively the lateral and vertical domain sizes.

The effectiveness of this scheme was tested by applying it to the internal wave system created by a point vortex (a multiple-frequency analogue of the vibrating-cylinder, 'Saint Andrew's cross', experiments of Mowbray & Rarity [27] (also in [28] and [29]), to verify that the internal waves neither re-entered the domain or reflected off the fringe boundaries. The energy absorbed by the fringe was calculated during the turbulent wake simulation. The strongest activity was detected during the NEQ phase of the simulation, when animations of quantities such as $\partial w/\partial z$ (cf. figure 12*b*) suggest that the waves are generated by individual turbulent structures (rather than, say, mean collapse of the wake defect associated with entry into the Q2D regime). For the present high-F flow, the internal-wave energy was found to be only a small percentage of the overall dissipation (see discussion regarding figure 3*b*).

Another computational challenge associated with this flow is defining an appropriate domain. The streamwise two-point correlations in figure 2*a* indicate that the streamwise domain size Λ_x is adequate throughout the simulation, and individual structures fit comfortably within the domain (since their streamwise integral scale is much smaller than Λ_x),

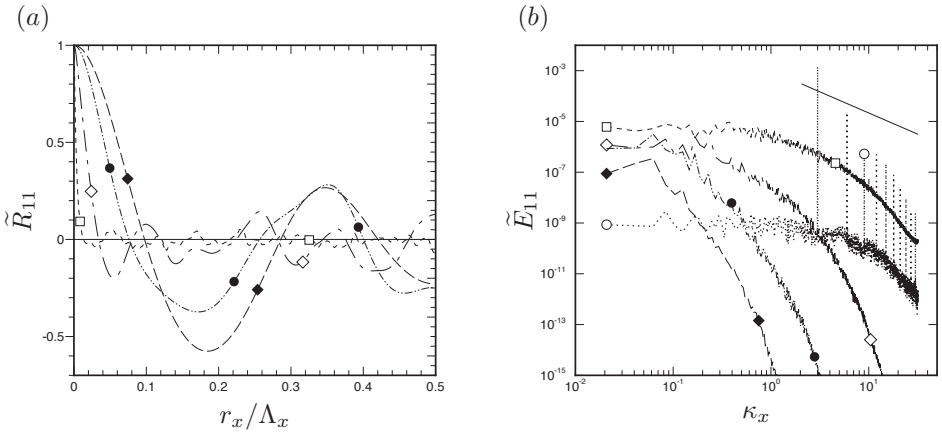

Figure 2. Evolution of (a) streamwise two-point autocorrelations and (b) streamwise spectra of streamwise velocity: ·····/○, $Nt = 0.2$ (in b only); - - - -/□, $Nt = 3.2$; ——/◇, $Nt = 21$; —·—/●, $Nt = 136$; — — —/⧫, $Nt = 587$. Straight solid line in (b) indicates $\kappa_x^{-5/3}$ behavior. Spectra $\widetilde{E}_{11}$ and correlations $\widetilde{R}_{11} = \widetilde{Q}_{11}/\widetilde{Q}_{11}(0)$ are from averages of E_{11} and Q_{11} over lateral and vertical planes though the wake centerline in regions for which $\overline{u} \geq 0.5\,U_d$, where $\overline{u'u'} = \sum_{\kappa_x} E_{11}(\kappa_x)$ and $Q_{11}(r_x) = \overline{u'(x)u'(x+r_x)}$. Spectra and wavenumbers in (b) normalized by $U_r = 2.09U_{do}$ and $L_r = h_o$.

even at very late times. The large-scale waviness during the late stages is due to the relatively low Reynolds number (i.e. narrow range of streamwise scales), and especially the periodicity of the large pancake-eddy structures present in the Q2D regime (figure 6). However, the streamwise domain size also directly affects the quality of the mean statistics (and possibly the dynamics of the merging of the large-scale structures), since it defines the size of the 'large-eddy sample' (which will decrease as time passes) that enters the streamwise mean. Therefore, the choice was made to have a relatively large streamwise extent, with $\Lambda_x/h_o = 96\pi \approx 302$ (cf. Gourlay *et al.*'s [13] $\Lambda_x/h_o = 245$, Brucker & Searcher's [9] $\Lambda_x/h_o \approx 105$, and Diamessis *et al.*'s [2] $\Lambda_x/h_o \approx 54$).

The possibility that the height and especially the width of the wake will outgrow the periodic domain is of even greater concern. To avoid this problem, without unduly wasting computational resources, the lateral and vertical domain sizes Λ_y and Λ_z are dynamically increased at appropriate times during the run, by projecting the periodic solutions onto a domain of greater extent in y, and lesser in z, with the same grid spacing. Details of this re-projection procedure are given in RCC. The spatial resolution is also reduced at certain times during the simulations, as allowed by the monotonically decreasing Reynolds number (see table 1).

The choices for the lateral and vertical domain are tabulated in table 1, with respect to both the initial h_o and local mean lateral h_y and vertical h_z half-widths. The criterion found by RCC for the unstratified case, that the lateral and vertical width h must remain less than 0.17 of the corresponding domain size, is satisfied throughout the simulation. Confirmation that stratification does not significantly alter this guideline is provided in figure 3a, where the DNS histories are given along with those from a test run identical to the case defined in table 1, except that the lateral and vertical domain sizes remain fixed at their values at $Nt = 28$ (corresponding to the end of the NEQ regime). There is good agreement between the two runs (including for the maximum U_d, width h_y and height h_z of the mean defect, as well as the streamwise u', lateral v' and vertical w' velocity fluctuations) until $Nt \approx 340$, at which point $h_y/\Lambda_y \approx 0.15$ and $h_z/\Lambda_z \approx 0.12$ for the smaller/fixed-domain results. These

Nt	M_x	$\Delta x/\eta_{\min}$	M_y	$\Delta y/\eta_{\min}$	Λ_y/h_o	h_y/Λ_y	$\Delta y/h_y$	M_z	$\Delta z/\eta_{\min}$	Λ_z/h_o	h_z/Λ_z	$\Delta z/h_z$
0	3072	3.8	256	1.0	2π	0.159	0.02	256	1.0	2π	0.159	0.02
0.87		7.0		1.7		0.155	0.02		1.7		0.157	0.02
0.87			384		3π	0.103	0.02	384		3π	0.105	0.02
1.12		6.7	256	2.5		0.112	0.02	256	2.5		0.110	0.02
1.12			384		4.5π	0.075	0.02	384		4.5π	0.073	0.02
2.86		2.9	256	1.6		0.131	0.02	256	1.6		0.120	0.02
2.86			384		6.75π	0.087	0.02	384		6.75π	0.080	0.02
5.38		1.8	256	1.5		0.132	0.02	256	1.5		0.087	0.03
5.38			384		10.13π	0.088	0.02				0.087	0.03
9.72	2560	1.4	256	1.5		0.108	0.02	192	1.3		0.085	0.04
9.72			384		15.19π	0.072	0.02				0.085	0.04
18.6	2304	1.0	256	1.4		0.078	0.03		0.8		0.078	0.05
18.6			384		22.78π	0.052	0.03				0.078	0.05
28.1	1536	1.2	320	1.4		0.057	0.04	128	1.0		0.077	0.07
28.1			480		34.17π	0.038	0.04	192		10.13π	0.052	0.07
35.4	1024	1.7	384	1.6		0.040	0.04		1.0		0.051	0.07
46.1	512	3.3	256	2.4		0.045	0.06	128	1.4		0.051	0.10
66.0	384	4.3	192	3.0		0.051	0.07	96	1.8		0.052	0.13
66.0			256		45.56π	0.038	0.07	128		13.5π	0.039	0.13
109		3.5	192	3.4		0.066	0.05	96	2.0		0.049	0.14
109			256		60.75π	0.050	0.05	128		18.0π	0.037	0.14
215	256	3.1	192	2.6		0.072	0.05	96	1.5		0.056	0.12
215			256		81π	0.054	0.05	128		24π	0.042	0.12
587		1.5		1.3		0.081	0.03		0.8		0.067	0.08
841		1.3		1.1		0.094	0.03		0.6		0.079	0.07

Table 1. Numerical parameters. The numbers of streamwise M_x, lateral M_y and vertical M_z Fourier-expansion coefficients are two-thirds of the corresponding collocation/quadrature points: $N_x = 3M_x/2$, $N_y = 3M_y/2$ and $N_z = 3M_z/2$. Streamwise Δx, lateral Δy and vertical Δz grid spacings given by Λ_x/N_x, Λ_y/N_y and Λ_z/N_z, respectively. Minimum Kolmogorov length scale $\eta_{\min} = (\nu^3/\epsilon_{\max})^{1/4}$, where $\epsilon_{\max}$ is the maximum of the streamwise-mean rate of dissipation of TKE at each time. The length Λ_x of the streamwise domain is fixed at $96\pi h_o$, where h_o is the mean wake half-width/height at $Nt = 0$, while Λ_y and Λ_z increase at times shown (indicated by vertical gaps between rows). Values remain unchanged until a new entry is given.

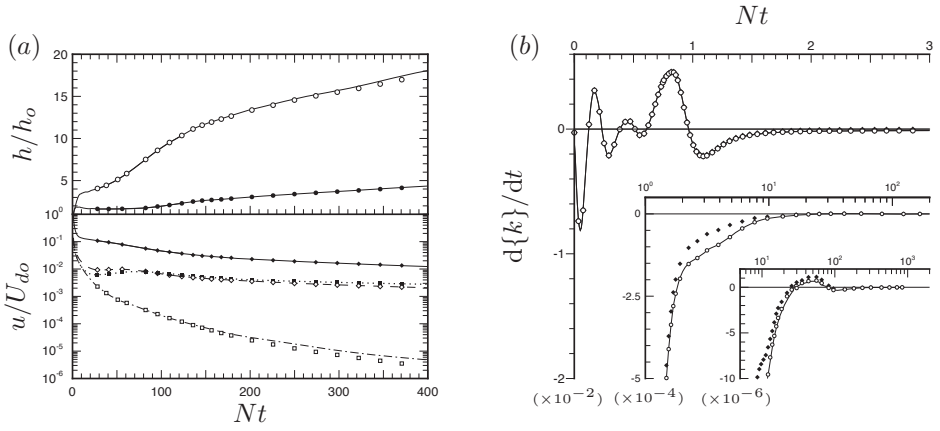

Figure 3. (a) Comparison of results from the present DNS and a fixed-domain test run beginning from $Nt = 28.1$, with Λ_y and Λ_z maintained at $34.17\pi h_o$ and $10.13\pi h_o$, respectively, such that the domain is not expanded at $Nt = 66$, 109 and 215; see table 1): lines, present DNS; symbols, fixed-domain test run ($\circ$, h_y; $\bullet$, h_z; $\blacklozenge$, U_d; $\diamond$, $\langle\overline{u'u'}\rangle^{1/2}$; $\blacksquare$, $\langle\overline{v'v'}\rangle^{1/2}$; $\square$, ($\langle\overline{w'w'}\rangle^{1/2}$, where streamwise $\langle\overline{u'u'}\rangle$, lateral $\langle\overline{v'v'}\rangle$ and vertical $\langle\overline{w'w'}\rangle$ Reynolds stresses are cross-wake averages over the region in the y-z plane where $\overline{u} > 0.05U_d$). (b) Histories from the present DNS of the rate of change of integrated TKE $\{k\}$ and net production minus dissipation plus buoyancy $\{\mathcal{P}_{\mathsf{tke}}\} - \{\epsilon_{\mathsf{tke}}\} + \{\mathcal{B}_{\mathsf{tke}}\}$ (see § 3.5 for definitions): ———, $\mathrm{d}\{k\}/\mathrm{d}t$; $\blacklozenge$, $\{\mathcal{P}_{\mathsf{tke}}\} - \{\epsilon_{\mathsf{tke}}\}$; $\circ$, $\{P_{\mathsf{tke}}\} - \{\epsilon_{\mathsf{tke}}\} + \{\mathcal{B}_{\mathsf{tke}}\}$. Budget terms in ($b$) given in units of $U_r^3 L_r$, where reference velocity $U_r = 2.09U_{do}$ and length $L_r = h_o$.

ratios are larger than those produced by the expansions used for the NEQ and Q2D phases of the present DNS, which implies the results have not been adversely affected by a too-small domain.

Table 1 also shows the changes in resolution over the course of the simulation. The streamwise Δx, lateral Δy and vertical Δz grid spacings are small enough multiples of the minimum Kolmogrov scale $\eta_{\min}$ throughout the simulation (between 1 and 4, except for a brief period at very early times when Δx reaches $7\eta_{\min}$) that we can safely assume the results faithfully capture all the significant spatial scales of the turbulence. The temporal scales are resolved by ensuring the Courant-Friedrichs-Lewy (CFL) number does not exceed $\sqrt{2.8}$. These conclusions are supported by the streamwise spectra in figure 2b. The signature of the vortex-ring characterize is apparent at $Nt = 0.2$. The spectra also indicate the moderate Reynolds number range considered here, in that $\kappa^{-5/3}$ behavior is apparent, but only at early times, bracketing $Nt = 3$. A more empirical check of the resolution is provided by the histories in figure 3b, comparing the sum of the production, dissipation and buoyancy terms (the fringe contribution is not included) in the integrated TKE equation (the open circles) with its integrated rate of change (solid line). The good agreement between the two points to the accuracy of the present DNS. It also implies that the energy of the internal waves generated by the turbulence during the NEQ phase is negligible, since the integral of the flux-divergence terms is essentially zero compared to that of the production, dissipation and buoyancy. This is in contrast to the low-F case, where departure from the 3D regime is accompanied by significant TKE transfer away from the wake (Brucker & Sarkar [9]).

We note that figure 3b also reveals the integrated buoyancy term (the difference between the solid diamonds and open circles) is negligible except between $Nt \approx 1.5$ and 15, and that during this time it acts solely as a sink of TKE. This provides an answer to the question raised in the introduction, regarding the defining NEQ mechanism, since it indicates that the transition from the 3D to the NEQ regime is not accompanied by a net transfer of

potential to kinetic energy.

A final comment regarding the present simulation strategy is warranted: the lateral- and vertical-domain expansion is accompanied by a coarsening of the resolution across the mean wake profiles $\overline{u}(y, z_0)$ and $\overline{u}(y_0, z)$, quantified in table 1 by a tendency for $\Delta y/h_y$ and $\Delta z/h_z$ to increase with time. A check was made that the loss of resolution does not compromise the shape of the $\overline{u}$ profiles, by repeating the portion corresponding to the largest Δz ($> 0.1h_z$, approximately) with double M_z, and confirming that the $\overline{u}$ results have negligible differences compared to those shown below.

3 Results

3.1 Flow visualisation

The turbulence structures associated with the 3D, NEQ and Q2D regimes are shown, respectively, in figures 4, 5 and 6. The weak stratification used here allows the wake turbulence to develop a mature three-dimensional state before buoyancy begins to alter the flow. At the time shown in figure 4 ($Nt \approx 3$) the stratification causes the height to be slightly smaller than the width (see also upper right-hand-side inset plot in figure 21*b*). However, it is evident that there is a substantial range of scales (cf. figure 2*b*), and that the wake is to a good approximation still axisymmetric.

The large-scale lateral oscillation, as well as the flattening and vertical striations, observed in the NEQ structure (figure 5, for $Nt \approx 21$) are typical of those found in other experiments and simulations [2, 12, 30], some of which correspond to lower F_∞ and higher R_∞. In contrast to the more isotropic eddies seen at $Nt = 3$, here the turbulence in figure 5 contains 'arrowhead' structures in the vertical plane through the wake centerline that point in the direction of motion of the virtual body associated with the wake (cf. figures 10–12 of Diamessis *et al.* [2]). A visual estimate of the height of the turbulent region (as opposed to that of the mean profile) indicates it is similar to, perhaps slightly less than, that for the 3D regime (compare figure 4*b*). The change in structure corresponds to enhanced production of TKE and profound anisotropy in its rate of dissipation (figure 16*b*). The lateral vorticity contours in figure 5*b* suggest the presence of Kelvin-Helmholtz (K-H) billows at the top and bottom of the wake, in the inclined shear layers of the arrowhead structures (e.g. near $x = 90h_o$). Diamessis *et al.* [2] discuss the manner in which the characteristics of these inclined shear layers depend upon Reynolds number, and the associated question of the how the layers' overturning via K-H instabilities can contribute to the generation of turbulence in stably stratified environments at high Reynolds number. For the present case, we show below that at the time corresponding to figure 5, viscous effects are not insignificant.

The Q2D regime contains flattened, large-scale, pancake- type motions in horizontal planes, such as those shown for $Nt \approx 587$ in figure 6. There are three separate vortical structures that have the two-layered feature that emerged earlier in the simulation (figure 5*c*), which bring to mind Godeford & Cambon's [11] distinction between two-dimensional and two-component turbulence (see also Spedding [12]). These two-layer eddies are similar to those observed by Spedding [1] (for $Nt \geq 50$ and $F_\infty > 10$), by Gourlay *et al.* [13] ($Nt > 100$, $F_\infty > 150$), by Brucker & Sarkar [9] ($Nt = 125$, $F_\infty = 8$), and by Diamessis *et al.* [2] ($Nt = 70$, $F_\infty = 4$). Figure 6 is also consistent with the vertical layering of lateral vorticity fluctuations seen by Spedding [12] (at $Nt = 64$ for $F_\infty = 4$). In light of the vortex-ring initialization used here, which injects structures very different from the helical modes associated with the towed-sphere wake (cf. figure 5*a* of RCC), the present results add to the growing body of evidence that the Q2D eddies are unrelated to the type of instability by which the wake became turbulent (see also [2, 13]).

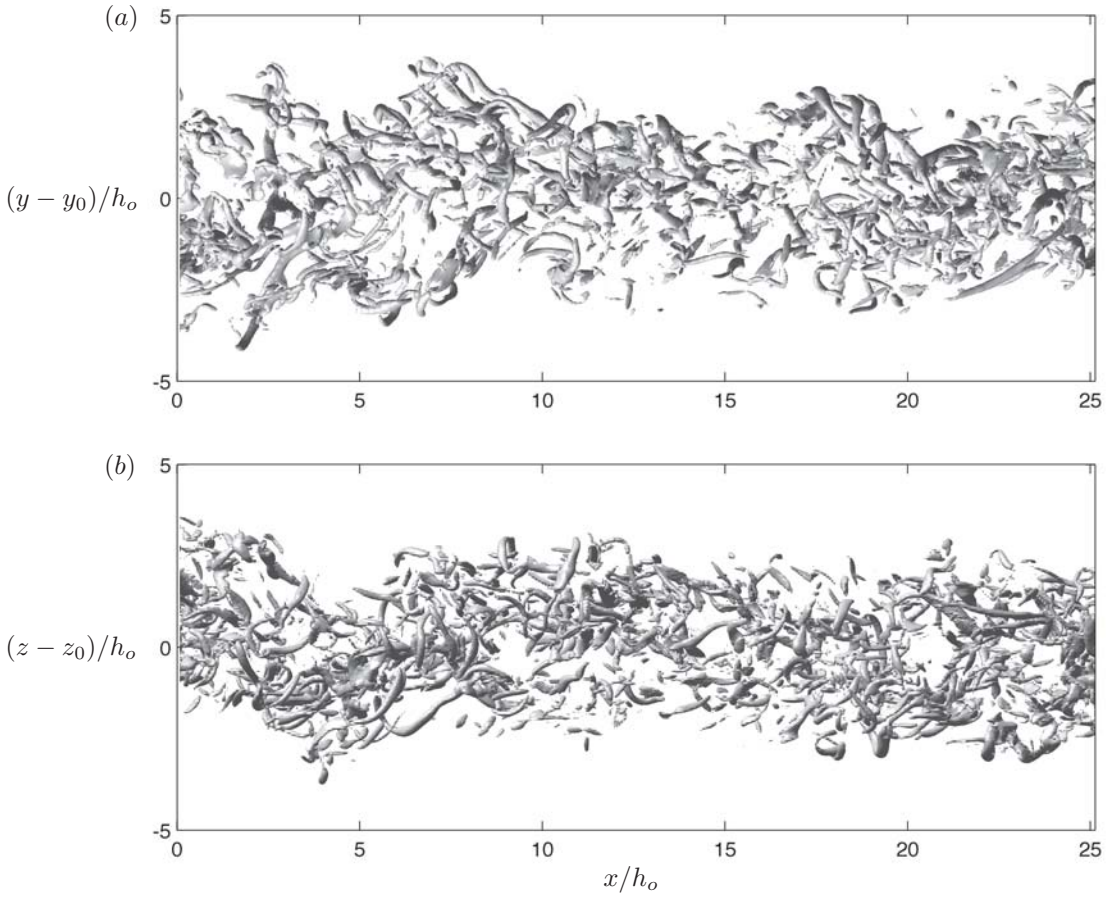

Figure 4. Instantaneous flow at $Nt = 3.2$ ($N\tilde{t} = Nt - Nt_{vo} = 2.5$, end of 3D regime; virtual origin t_{vo} defined in figure 7). (a) Top and (b) side views of isosurfaces of vorticity magnitude ($|\omega| = 0.38\,U_r/L_r$). Mean-flow direction defined as if a virtual wake-creating body has moved from left to right through the sub-domain shown. Views shown are 8% of streamwise, and 47% of lateral and vertical, domain.

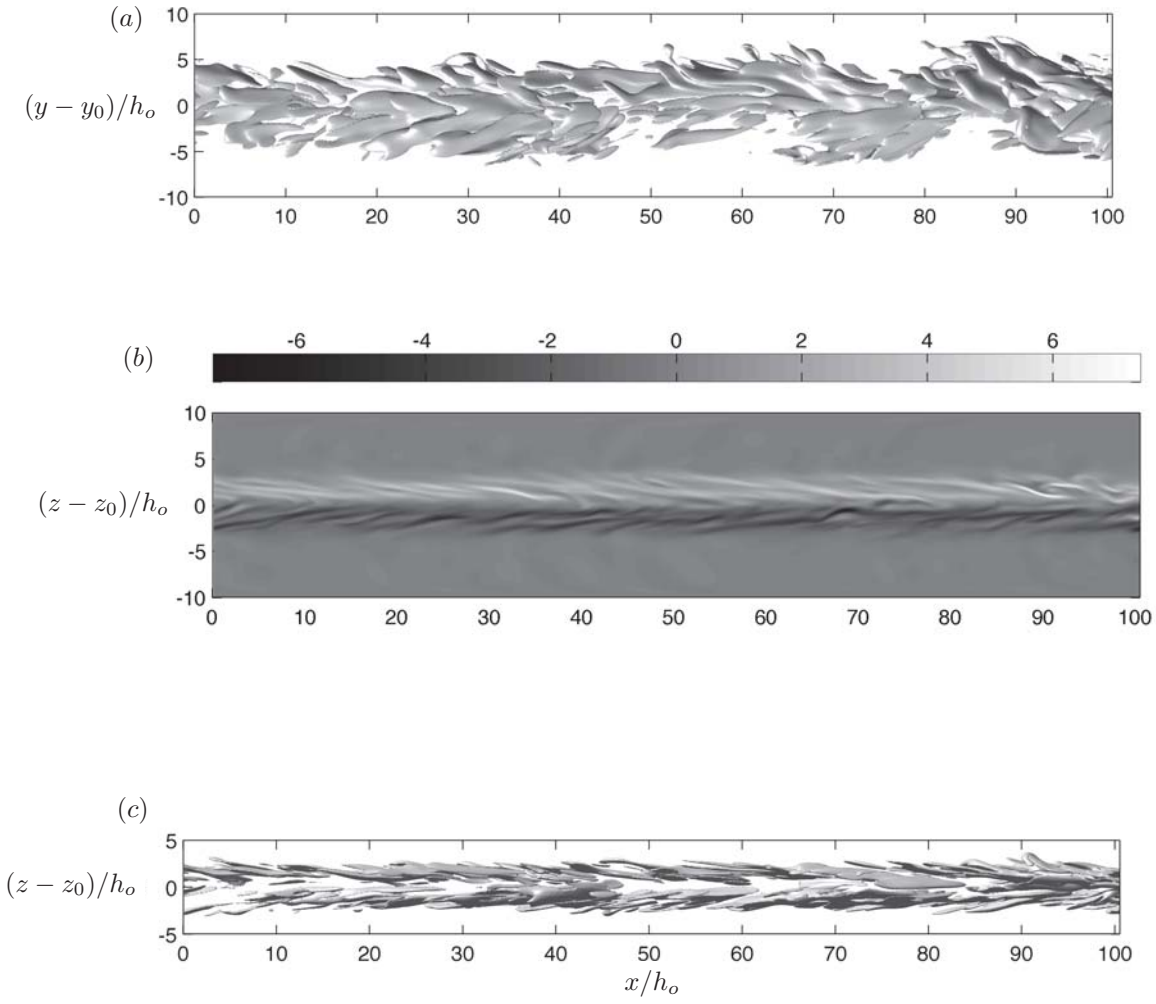

Figure 5. Instantaneous flow at $Nt = 20.9$ ($N\tilde{t} = Nt - Nt_{vo} = 20.2$, NEQ regime; virtual origin t_{vo} defined in figure 7). (a) Top and (c) side views of isosurfaces of vorticity magnitude ($|\omega| = 9.7 \times 10^{-4}\, U_r/L_r$) . ($b$) Contours of lateral vorticity ω_y in vertical plane through centerline, in units of $10^2 U_r/L_r$. Motion of virtual wake-creating body is from left to right. Views shown represent subregion of full domain (table 1).

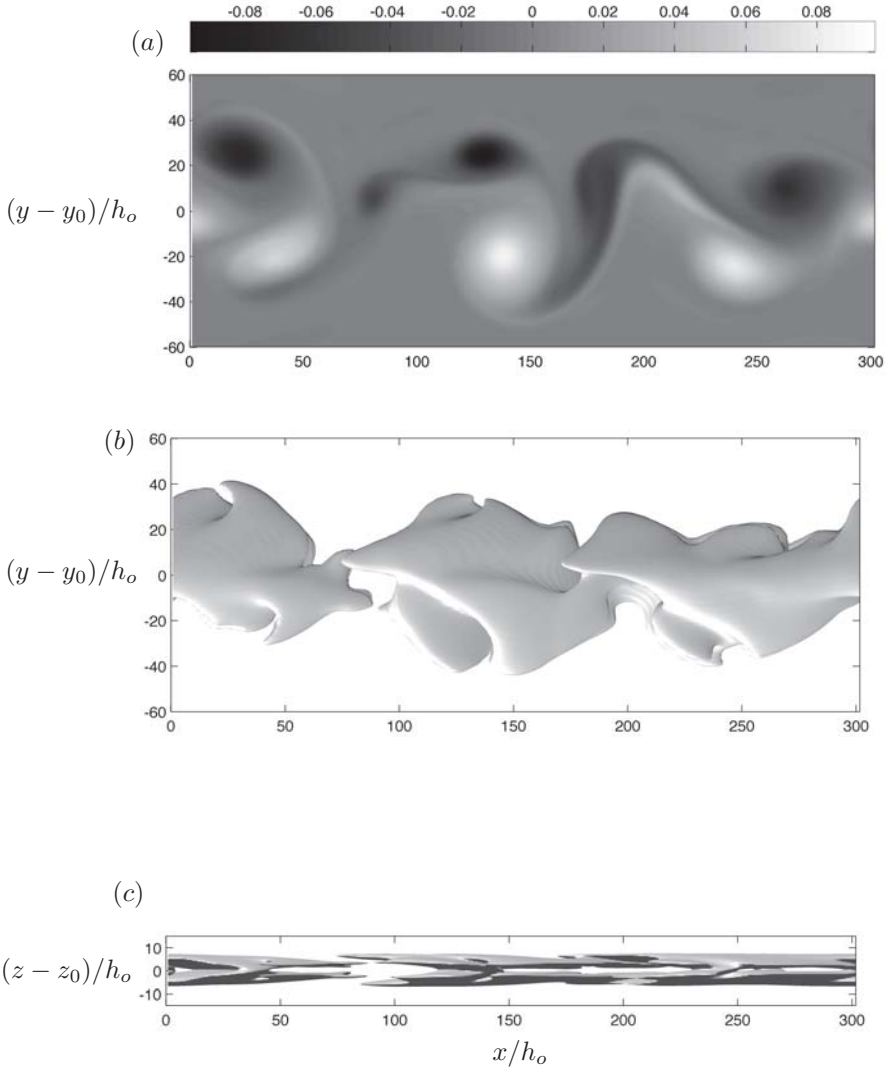

Figure 6. Instantaneous flow at $Nt = 586.9$ ($N\tilde{t} = Nt - Nt_{vo} = 586.2$, Q2D regime; virtual origin t_{vo} defined in figure 7). (a) Contours of vertical vorticity ω_z in horizontal plane through centerline, in units of $10^4 U_r/L_r$). (b) Top and (c) side views of isosurfaces of vorticity magnitude ($|\omega| = 3.1 \times 10^{-7}\, U_r/L_r$). Motion of virtual wake-creating body is from left to right. Views shown represent full streamwise, but subregions of lateral and vertical, domain (table 1).

3.2 Mean defect history

The history of the maximum mean velocity defect U_d is shown in figure 7*a* and *b*. The U_d variation is smoother than that typically found from simulations, due to the reduced statistical oscillations associated with the larger-than-usual streamwise domain used here (the same can be said for the mean-wake height and width histories in figure 7*c*, *d*). In contrast to the unstratified-wake DNS of RCC, for which the difference between the maximum and the centroid of the mean defect increased with time, and becomes significant at later stages, here there is essentially no difference between the two, for the time period considered. There is however a noticeable difference in the location in the y-z plane at which the two occur; as in RCC, we use the location of the centroid of the mean-velocity distribution $\overline{u}(y,z)$ to define the current/local wake centerline coordinates (y_c, z_c).

Figure 7*b* also shows histories of the streamwise u', lateral v' and vertical w' velocity fluctuations at the wake centerline (symbols). These, along with the U_d history, reveal that it is not until after $Nt \approx 1$ that the wake turbulence is fully developed. We therefore view the early phase, from $Nt = 0$ until $Nt = Nt_{vo} \approx 1$, as effectively a precursor simulation. The exact virtual-time origin t_{vo} is defined by the unstratified, 3D similarity diagnostic $U_d^{-3/2}$ shown in figure 7*a*, from which we deduce $Nt_{vo} = 0.645$ (chain-double-dotted line). In order to remove some of the uncertainty associated with comparing the present results during the 3D and NEQ regimes with those from experiments and other simulations, the histories that follow will be presented as functions of $N\tilde{t} = Nt - Nt_{vo} = Nt - 0.645$. Figure 7*a* also indicates that U_d continues to exhibit pure-3D behavior until $N\tilde{t} = Nt - Nt_{vo} \approx 4.8 - 0.645 \approx 4.2$, since this is when the similarity diagnostic first deviates from the linear variation.

The early wake is well represented by the canonical $U_d \sim t^{-2/3}$ history despite not being fully self similar during this time: although fully turbulent and essentially unstratified and axisymmetric (figure 8*a*), the wake's non-dimensional Reynolds-shear-stress profile in cylindrical coordinates $-\overline{v'_x v'_r}/U_d^2$ (not shown) is not solely a function of the non-dimensional radius r/h (i.e. with no time dependence). This is consistent with the evolution of the unstratified, vortex-ring-initialized, Case VR wake described in RCC, for which (non-universal) self-similarity did not appear until after the time corresponding to $Nt \approx 11$ for the present simulation – and universal self-similarity not until $Nt > 70$. (For the present DNS, the relationship between Nt and the non-dimensional time used in RCC is $t/t_* = 30Nt$.) In fact, in the range corresponding to $1 < Nt < 11$, the U_d history for Case VR decays as t^{-1}, because of the unique turbulence distribution induced by the Case VR rings (which produce an eddy viscosity profile that is temporally constant and radially uniform; see figures 8*a* and 9*b* of RCC). Here the ring initialization, which used somewhat larger streamwise spacing, $2.1h_o$ rather than Case VR's $1.85h_o$, is such that $U_d \sim t^{-2/3}$ is a better representation than t^{-1} for the 3D regime. These observations illustrate the profound impact the initial wake structure can have upon its development.

As observed elsewhere (e.g. in Spedding's [1] experiments and Gourlay *et al.*'s [13] simulation), the magnitude of the rate of decay $|\mathrm{d}U_d/\mathrm{d}t|$ slows markedly for $Nt > 5$, as the flow enters the NEQ phase, such that $U_d \sim t^{-n}$ with $n \leq 1/4$. In this region, the U_d variation is well represented by the interpolant $0.25(Nt+1)^{-1/4}$. (It should be mentioned that power laws with slightly different exponents could also reproduce the U_d decay to good accuracy, given the flexibility afforded by the use of a finite virtual origin for time.) The time at which the 3D and NEQ power laws intersect, $N\tilde{t} = Nt - Nt_{vo} \approx 6 - 0.645 \approx 5.5$, can be viewed as an estimate of the boundary between the two regimes for the present flow. The generality of this finding will be discussed in § 3.6.

The U_d history for the variable-viscosity run (Case R1500; see § 2) begins to significantly differ from the constant-viscosity/variable-R_d result after $N\tilde{t} \approx 100$ (compare dotted and solid lines in inset plot in figure 7*b*), which implies non-inertial effects are important after this time. The NEQ period revealed by the evolution of U_d begins at $N\tilde{t} \approx .5.5$ and

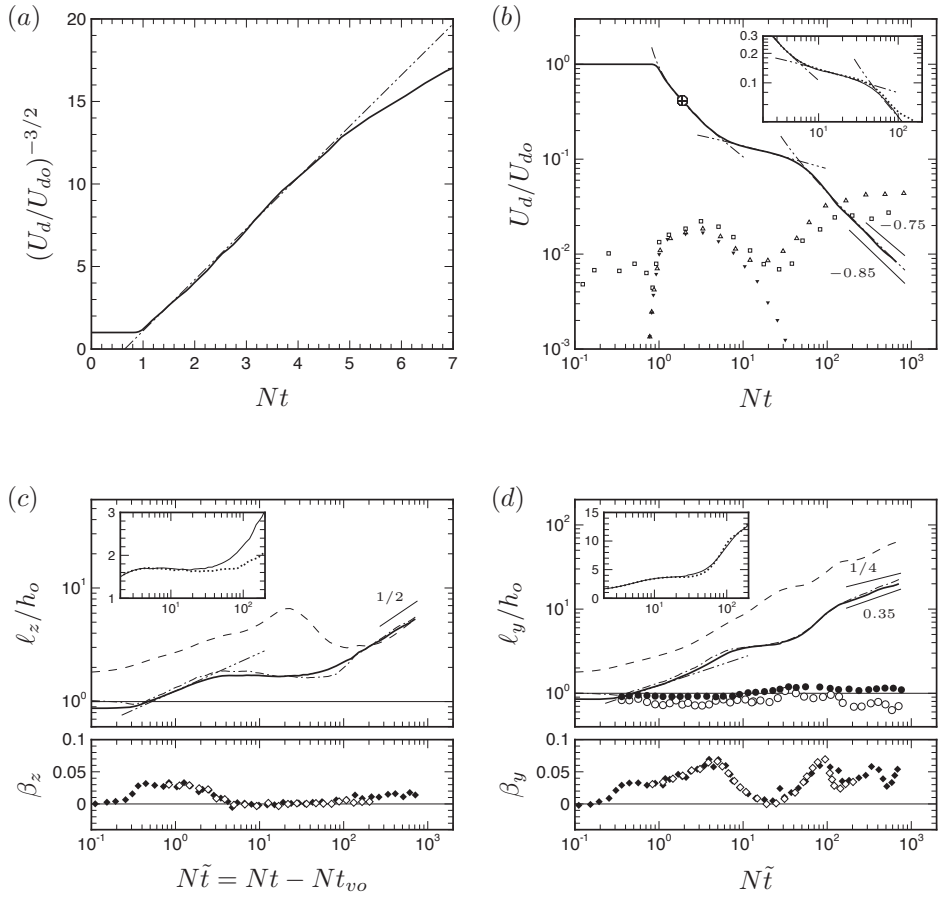

Figure 7. Histories of (a, b) maximum mean velocity U_d, (c) mean height ℓ_z and vertical spreading rate β_z and (d) mean width ℓ_y and lateral spreading rate β_y: ———, present DNS (with $\ell_z = r_z^*$ and $\ell_y = r_y^*$ in c and d, respectively); □ (in b only), $0.1(\overline{u'u'})_c^{1/2}/U_d$ (arbitrary factor of 0.1 is to aid visibility); Δ (in b only), $0.1(\overline{v'v'})_c^{1/2}/U_d$; ▼ (in b only), $0.1(\overline{w'w'})_c^{1/2}/U_d$; —·—(in c and d), h_z and h_y; - - - -(in c and d), r_z' and r_y'; ∘ (in d only), L_σ'/r_y^* (cf. Meunier & Spedding [17]); • (in d only), L_σ''/r_y^* (cf. Meunier & Spedding [17]); ♦, (in c) $\beta_z = (1/U_d)\mathrm{d}r_z^*/\mathrm{d}t$ and (in d) $\beta_y = (1/U_d)\mathrm{d}r_y^*/\mathrm{d}t$; ⋄, (in c) $\beta_z = (1/U_d)\mathrm{d}r_z^*/\mathrm{d}t$ and (in d) $\beta_y = (1/U_d)\mathrm{d}r_y^*/\mathrm{d}t$ for Case R1500 (variable-viscocity ($U_d\, r^*/\nu \geq 1500$) run); ——···——, curve fits for (a, b) U_d, (c) r_z^* and (d) r_y^*, where in (a) $(U_d/U_d(t))^{-3/2} = 3.1(Nt - 0.645)$, in (b) $U_d/U_{do} = 0.47(Nt - 0.645)^{-2/3}$ for $Nt < 10$, $U_d/U_{do} = 0.25(Nt + 1.0)^{-1/4}$ for $3 < Nt < 100$, $U_d/U_{do} = 2.05(Nt - 10)^{-0.85}$ for $Nt > 40$, while in (c) and (d) $r_z^*/h_o = r_y^*/h_o = 1.23(N\tilde{t})^{1/3}$ for $Nt < 10$ where $N\tilde{t} = Nt - Nt_{vo}$ and $Nt_{vo} = 0.645$ (see figure 21b). ⊕ (in b only), time at which Case R1500 first reaches its minimum Reynolds number, $U_d\, r^*/\nu = 1500$; ····· (inset plots in b, c, d only), Case R1500 (with $\ell_z = r_z^*$ and $\ell_y = r_y^*$ in c and d). At $Nt = 0$, $r_z^* = r_y^* = r_o^* = 0.865 h_o$. The $U_d(t)$ interpolants intersect at $Nt \approx 6$ and 45.

follows (or remains just above) the NEQ power-law curve fit until about $N\tilde{t} = 30$ and $N\tilde{t} = 50$ respectively for the constant- and variable-viscosity (i.e. lower and higher Reynolds number) cases. The effect of viscosity on the NEQ duration is even more apparent in the height histories (figure 7*c*). The Reynolds numbers for both cases are thus too low to allow an extended NEQ region – and that the period during which significant turbulence is 'regenerated' by Kelvin-Helmholtz instabilities (Diamessis *et al.* 2011), if it exists at all, will be quite brief (cf. figure 5*b*). (see instantaneous lateral vorticity contours at $N\tilde{t} = 20$ in figure 5 of Redford *et al.* 2014). The Reynolds-number dependence of the duration of the NEQ regime will be considered further in § 3.6. For now we note that the U_d history seen here during the final stage of the NEQ phase is more consistent with the $t^{-1/2}$ behavior of the 'buoyancy-controlled' subregion between NEQ and Q2D proposed by Meunier *et al.* (2006) than the U_d plateau of the 'NEQ^2' subregion identified by Brucker & Sarkar (2010).

A $t^{-3/4}$ power law for U_d could be assumed for the Q2D regime (cf. [3,25]), which would agree well with the present data for $Nt \geq 80$ if a virtual origin of $Nt = 30$ were used. (Recall the earlier comment about the interplay between the power law's exponent and virtual origin.) However, a better fit is provided by $t^{-0.85}$ for $Nt \geq 60$, with a smaller virtual origin ($Nt = 10$) (chain-double-dotted curve in figure 7*a*). The -0.85 exponent is also more consistent with conservation of mean momentum, when coupled with the behavior of the vertical and lateral defect dimensions (see below). The NEQ/Q2D boundary defined by the intersection of the corresponding power-law interpolants is $N\tilde{t} \approx 55$; the $t^{-0.85}$ interpolant closely corresponds to the U_d variation until the end of the (primary) simulation, $Nt \approx 840$. Note that the final time is not large enough for a purely viscous 3D regime to appear (such that $U_d \sim t^{-1}$; see Meunier *et al.* [3]). In fact, the TKE remains a significant fraction of U_d^2 for all the times considered here (figure 15*a* inset plot). Nevertheless, the importance of viscous effects during the Q2D phase is underscored by the significant deviation for $Nt > 90$ of the U_d histories from the constant- and variable-viscosity flows (figure 7*b* inset plot).

The height histories are shown in figure 7*c*. Both the 'half-radius' height h_z (i.e. half the distance between the locations at which the mean velocity in the vertical plane through the centerline, $\overline{u}(z, y_c)$, is 0.5 of U_d; *not* a best-fit to an assumed Gaussian profile), and an integral measure r_z^* are shown; the latter is defined as $r_z^* = [(2 \ln 2/U_d) \int_0^\infty \overline{u}(r_z, y_c) r_z \mathrm{d}r_z]^{1/2}$, where $r_z^2 = (z - z_c)^2$ and (y_c, z_c) are the coordinates of the local wake centerline. The integral height has been normalized such that it is equal to h_z when $\overline{u}(z, y_c)$ is Gaussian. Consequently, the greater the difference between h_z (chain-dotted line) and r_z^* (solid) in figure 7*c*, the more non-Gaussian the vertical mean velocity profile (figure 9*a*).

During the 3D phase, when the wake is effectively unstratified, its height and width grow in proportion to $\tilde{t}^{1/3}$, and its non-dimensional mean growth/spreading rate $\beta_z = (1/U_d)\mathrm{d}r_z^*/\mathrm{d}t$ is approximately constant. This can be seen in figure 7*c*, for $N\tilde{t} < 3$ (chain-dotted curve and symbols, which respectively trace a $\tilde{t}^{1/3}$ interpolant for r_z^* and the β_z variation). Perhaps unsurprisingly, given the flattening and widening effect the stratification has on the mean defect, the height/width interpolant deviates from the DNS sooner (near $Nt - Nt_{vo} = 2$) than the corresponding U_d power-law interpolant does ($N\tilde{t} \approx 4.5$).

Despite the wake not becoming fully self-similar, the spreading rate during the unstratified regime remains fixed near 0.03, which is roughly half that observed at much later times (corresponding to $Nt > 70$) for the self-similar growth of RCC's unstratified Case VR wake. The streamwise velocity fluctuations at the centerline are also weaker here during the 3D regime, than for Case VR during its (first, non-universal) fully self-similar phase, with $(\overline{u'u'})_c^{1/2}/U_d \approx 0.2$ here (open squares in figure 7*b*) compared to approximately 0.3 for Case VR.

The difference between the integral height for the constant- and variable-viscosity runs (solid and dotted curves, respectively, shown in inset plot), and that of the non-dimensional mean growth/spreading rate β_z (solid and open diamonds) – namely that the region of zero

slope (and thus zero β_z) lasts longer for larger R_d ($N\tilde{t} \approx 70$ rather than 30) – corroborate Meunier *et al.*'s [3] prediction, and Diamessis *et al.*'s [2] observation, that the duration of the NEQ regime increases with increasing Reynolds number.

Figure 7*c* also shows the differences in the evolution of the height of the mean defect and vertical extent of the wake turbulence, which become apparent when one compares histories of h_z (chain-dotted curve) or r_z^* (solid) with that of r_z' (dashed), a TKE based integral length, defined as $r_z' = \left(\{k\,(z-z_c)^2\}/\{k\}\right)^{1/2}$ where $k = \frac{1}{2}\overline{u_i' u_i'}$. The mean defect does indeed 'collapse' early in the NEQ regime, in the sense that both h_z and r_z^* decrease with time from $N\tilde{t} \approx 8$ until about $N\tilde{t} = 15$ – although the reduction in the integral height is much weaker than that exhibited by the $\overline{u} = 0.5U_d$ measure h_z. As found by Gourlay *et al.* [13], the turbulent region continues to spread vertically during the NEQ regime, when $\mathrm{d}r^*/\mathrm{d}t \approx 0$, before an even more dramatic collapse occurs, with $\mathrm{d}r_z'/\mathrm{d}t < 0$ (much larger than the negative $\mathrm{d}h_z/\mathrm{d}t$ and $\mathrm{d}r_z^*/\mathrm{d}t$ seen earlier) between $N\tilde{t} \approx 20$ and 100. This behavior was also observed for the self-propelled case by Lin & Pao [10] in their flow-visualisation experiments, and in Brucker & Sarkar's [9] DNS of self-propelled and towed wakes.

After the wake enters the Q2D regime, r_z' begins to grow again, as do h_z and r_z^*. All three heights then converge, as the vertical spreading becomes a purely viscous phenomenon, such that $h_z \approx r_z^* \approx r_z'$ [13] and each grow as $t^{1/2}$ [3]. This can be seen in figure 8, which includes contours of the mean defect (lines) and TKE (colour) at times representing the three regimes. The tendency for the height of the turbulent region to occupy a smaller and smaller fraction of the mean defect as time passes is clear. (The changes to the TKE budget corresponding to the change in shape of the TKE profiles – for example, the growth of the 'flattened, double-pronged' structure in the y-z plane that begins to appear during the NEQ phase – will be considered in § 3.5.) The non-dimensional vertical growth rate β_z is therefore positive but much smaller than during the 3D regime, when the spreading is effected by the turbulence.

Due to the conservation of mean streamwise momentum, the product of the mean height, width and maximum velocity will remain approximately constant through the wake's lifetime. (It would be exactly constant for a pure 2D-Gaussian mean defect. The $U_d h_z h_y$ product for the primary simulation remains within $\pm 16\%$ of its value at $Nt = 1$ for the full $1 \leq Nt \leq 840$ range.) The variations of the power-law exponents for U_d and h_z during the 3D, NEQ and Q2D regimes are thus expected to lead to variations for the mean-width history (which would conflict with Diamessis *et al.*'s [2] claim that $h_y \sim t^{1/3}$ for all three regimes). For example, the combination of monotonically decreasing U_d and $\mathrm{d}r_z^*/\mathrm{d}t \to 0$ requires the mean width to grow faster than it does during the 3D phase as the wake enters the NEQ regime. Figure 7*d* illustrates the enhanced lateral growth, compared to the 3D power law (chain-double-dotted curve), in terms of both the mean half-width/radius h_y (chained-dotted curve) and the integral width $r_y^* = [(2\,\ln 2/U_d)\int_0^\infty \overline{u}(z_c, r_y) r_y \mathrm{d}r_y]^{1/2}$, with $r_y^2 = (y - y_c)^2$ (solid curve), for $1.5 \leq N\tilde{t} \leq 4.5$. Thereafter, the rate of spreading slows, falling from a maximum near $N\tilde{t} = 5$ to a local near-zero minimum near $N\tilde{t} = 20$ (see open and closed diamonds in figure 7*d*, which show the history of the non-dimensional lateral spreading rate $\beta_y = (1/U_d)\mathrm{d}r_y^*/\mathrm{d}t$). Beginning from $N\tilde{t} \approx 25$, as the wakes leaves the NEQ and enters the Q2D regime (and $U_d(t)$ begins to increase its rate of decay), the lateral growth increases rapidly until it reaches a value comparable to that observed during the unstratified 3D period, with $r_y^* \sim t^{0.35}$. This is similar to the $h_y \sim t^{1/3}$ proposed by Diamessis *et al.* [2], but differs from the $t^{1/4}$ included in Meunier *et al.*'s [3] model, and the $t^{0.23}$ observed in Brucker & Sarkar's [9] DNS, for the Q2D range. The difference between the $n = 0.35$ and 0.25 exponents is shown by the thin-solid lines in figure 7*d*, which supports our preference for the larger value – which in turn explains (in light of the viscous $n = 1/2$ growth of h_z, and conservation of momentum) our use of $n = -0.85$ to fit the $U_d(t)$ history (figure 7*b*). (Meunier *et al.*'s [3] exponent combination of $(-3/4, 1/2, 1/4)$ for (U_d, h_z, h_y)

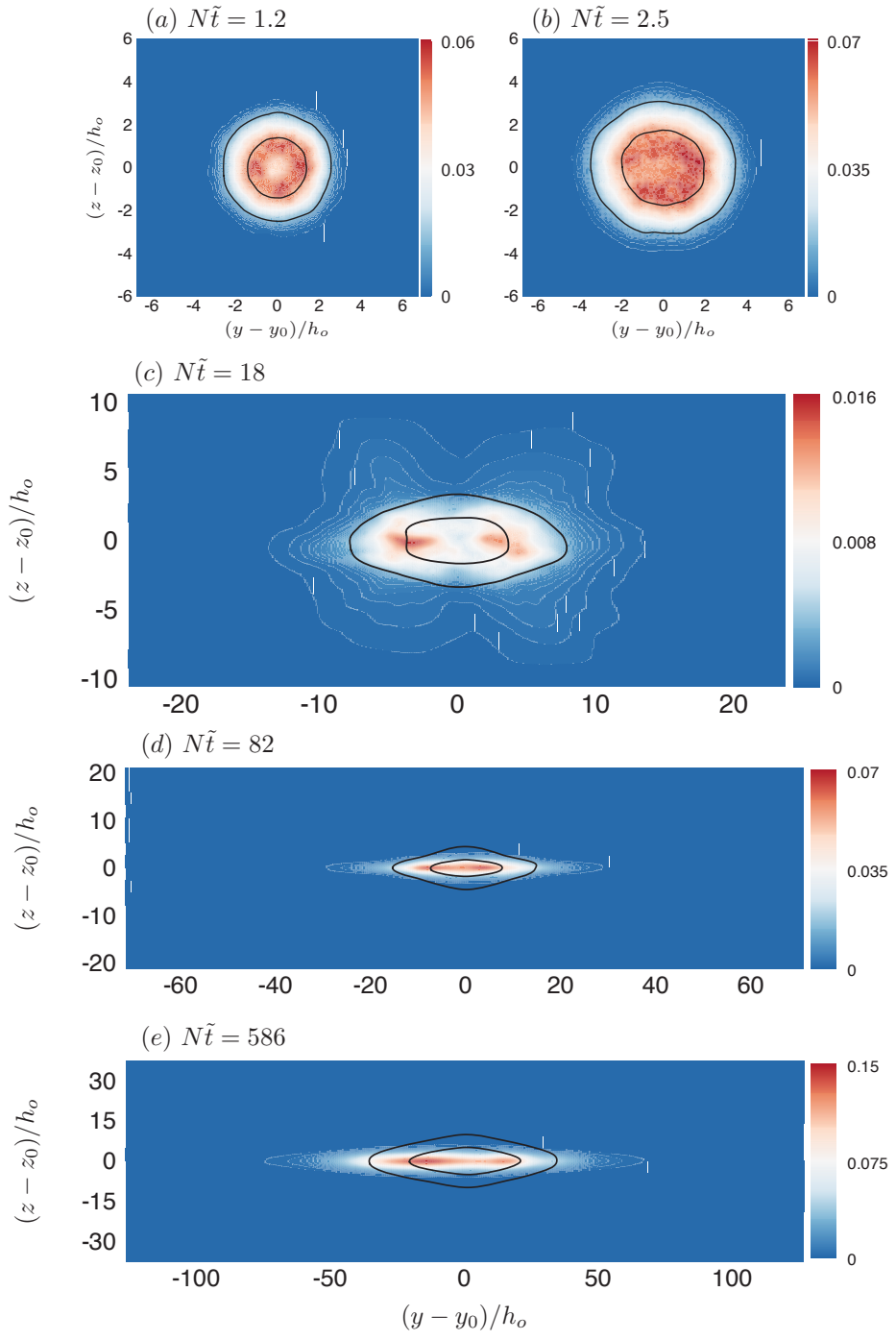

Figure 8. Mean-defect and TKE contours at: (*a*) $N\tilde{t} = 1.2$, (*b*) $N\tilde{t} = 2.5$, (*c*) $N\tilde{t} = 18$, (*d*) $N\tilde{t} = 82$ and (*e*) $N\tilde{t} = 586$. TKE (shaded contours) normalized by local U_d^2. Solid-line contours correspond to $\overline{u} = 0.05U_d$ and $0.5U_d$.

also satisfies the constant-momentum constraint.) Despite the profound qualitative differences in the turbulence structure in the 3D and Q2D regimes, the rate at which the mean defect spreads laterally is about the same.

The width of the turbulence, like that of the mean defect, grows continuously throughout the lifetime of the wake. This can be seen by the history of the TKE-based integral width $r'_y = \left(\{k\,(y-y_c)^2\}/\{k\}\right)^{1/2}$ in figure 7*d* (dashed line). In contrast to the height of the turbulent region, its width remains significantly larger than the width of the mean defect, with $r'_y/h_y > 1$ for each of the 3D, NEQ and Q2D periods (cf. Gourlay *et al.* [13]). (We cannot say whether or not the waviness in $r'_y(t)$ for $N\tilde{t} > 20$ is physical.) The closed and open circles in figure 7*d* respectively correspond to the ratios L'_σ/r^*_y and L''_σ/r^*_y, where L'_σ and L''_σ are, respectively, the distance from the wake centerline to the maximum values of the lateral Reynolds shear stress $-\overline{u'v'}$ and the horizontal-plane velocity fluctuations $(\overline{u'u'} + \overline{v'v'})^{1/2}$. Integral version of these scales are used, based on the profiles presented in Meunier & Spedding [17], with $L'_\sigma = \int_{-\infty}^{\infty} |\overline{u'v'}|\mathrm{d}y/u_0^{'2}$ and $L''_\sigma = \int_{-\infty}^{\infty} (\overline{u'u'} + \overline{v'v'})^{1/2}\mathrm{d}y/(2\pi)^{1/2}u_0^{''}$, where $u_0^{'2} = \exp(0.5)(\overline{u'v'})_{\max}$, $u_0^{''} = 0.5\exp(0.5)(\overline{u'u'} + \overline{v'v'})^{1/2}_{\max}$, and $(\overline{u'v'})_{\max}$ and $(\overline{u'u'} + \overline{v'v'})^{1/2}_{\max}$ are the maxima over y of $|\overline{u'v'}|$ and $(\overline{u'u'} + \overline{v'v'})^{1/2}$, respectively.

In contrast to r'_y/r^*_y, which is always significantly greater than one, the shear-stress width ratio L'_σ/r^*_y remain close to unity for the entire run, slightly less before $N\tilde{t} \approx 10$, slightly more thereafter, while for the horizontal TKE measure $0.7 < L''_\sigma/r^*_y \leq 1$ throughout. The $L'_\sigma \approx r^*_y$ and $L''_\sigma \approx r^*_y$ behavior, which is similar to that exhibited by the experimental data for various bluff bodies given in Meunier & Spedding [17], implies a type of self-similarity for the lateral profiles, especially for $-\overline{u'v'}$, that survives as the importance of stratification and viscous effects grows, and the flow moves through the 3D, NEQ and Q2D regimes.

The decoupling of the vertical and lateral spreading processes, and the associated greater importance for the latter of the mixing due to turbulence relative to molecular viscosity, is illustrated by the much closer agreement of the mean width r^*_y from the constant- and variable-viscosity flows (figure 7*d* inset) compared to the corresponding r^*_z histories (figure 7*c* inset).

Figure 9 contains vertical (9*a*) and lateral (9*b*) profiles of streamwise-mean velocity $\overline{u}$, normalized by the local maximum U_d and height h_z or width h_y of the defect. The better collapse and smoother profiles seen here, compared to those from Gourlay *et al.*'s [13] DNS and Diamessis *et al.*'s [2] LES, are thought to be a symptom of the better averaging sample afforded by the present larger streamwise domain. Included in these plots are results from times correspond to the structures shown in figures 4 (dashed curve; 3D regime), 5 (chain-dashed; NEQ) and 6 (long-dashed; Q2D). (The dotted profile is the mean induced by the vortex ring initialization.) Given the qualitative differences in the 3D, NEQ and Q2D structures, the collapse at these times is striking, as is the agreement with the Gaussian idealization (open symbols), particularly near the centerline. At the earlier times, the non-Gaussian behavior away from the centerline may be an artifact of the vortex-ring initialization, and/or due to attenuation of the eddy viscosity, associated with corrugations of the interface between the vortical and irrotational regions [31] (figure 4).

For the lateral profiles, which tend to be more consistently Gaussian than the vertical ones, the near-centerline agreement is similar to that found by Spedding *et al.* [25]. (The unphysical lateral asymmetry at $N\tilde{t} = 137$ is evidence of finite eddy sample at this time. Curiously, the $\overline{u}(z_c, y)$ profile at $N\tilde{t} = 586$, which is the result of averaging over an even smaller number of eddy structures than are present at $N\tilde{t} = 137$, is nearly exactly symmetric; see long-dashed curve in figure 9*b*.) The vertical profiles, on the other hand, can at times exhibit significant non-Gaussian features, across the entire wake. One might suspect the 'extra peakiness' near the centerline during the early stages of the Q2D regime ($N\tilde{t} = 82$ and 137) is due to the coarsening of the vertical resolution across the mean defect (i.e. $\Delta z/h_z = 0.14$; cf. table 1) mentioned at the end of § 2. However, this possibility was ruled

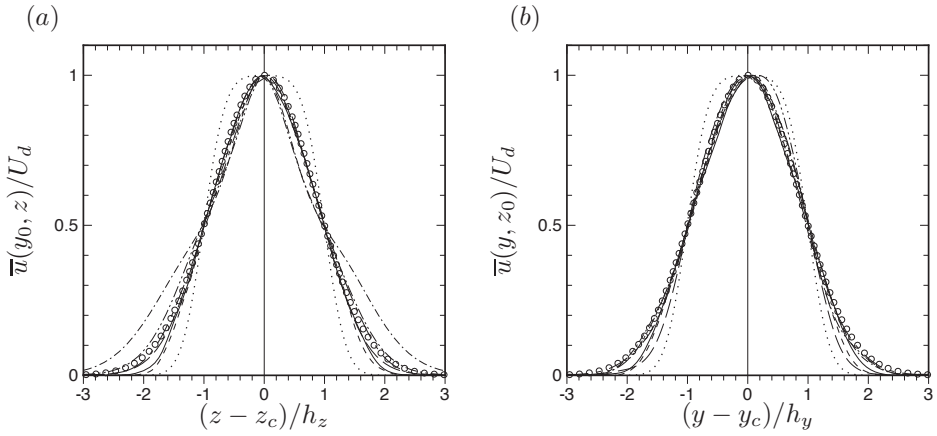

Figure 9. Profile of mean streamwise velocity in (a) vertical and (b) lateral planes through the wake centerline: ·····, $Nt = 0$; ——, $N\tilde{t} = 1.2$ – – –, $N\tilde{t} = 2.5$; —·—, $N\tilde{t} = 20$; —·—, $N\tilde{t} = 82$; —··—, $N\tilde{t} = 137$ — — —, $N\tilde{t} = 586$; ∘, Gaussian idealisation $\overline{u}/U_d = \exp(-\ln(2)\, s^2)$, where s is either $(y - y_c)/h_y$ or $(z - z_c)/h_z$. Coordinates (y_0, z_0) and (y_c, z_c) respectively define the initial and current location of the wake centerline, given by the centroid of the mean velocity defect.

out by repeating this portion of the simulation with increased M_z, such that $\Delta z/h_z = 0.07$, resulting in $\overline{u}(z, y_c)$ variations that are nearly indistinguishable to those shown in figure 9a.

The mechanisms responsible for the evolving shape of the mean defect revealed in figure 9, as well as its magnitude, height and width (figure 7), can be further understood by examining the corresponding evolution of the terms in the mean-momentum transport equation. But before attending to that task, we consider the history and budget of mean kinetic energy.

3.3 Integrated mean kinetic energy history and budget

The effect of the stably stratified background upon the three components of mean kinetic energy (MKE) is illustrated in figure 10a. Histories of the (cross-domain) area-integrated quantities $\{K_{\alpha\alpha}\} = \{\frac{1}{2}\overline{u}_\alpha\overline{u}_\alpha\}$ for $\alpha = 1, 2, 3$ (no sum on α) are shown. Only during the NEQ regime are the lateral and vertical energies non-negligible compared to the streamwise component, and even then $\{K_{11}\}$ remains at least 1.5 orders of magnitude larger than $\{K_{22}\}$ and $\{K_{33}\}$. After $N\tilde{t} \approx 3$, the buoyancy suppresses the vertical component compared to the lateral one, and there is a net transfer of energy from the vertical mean kinetic energy K_{33} to the mean potential energy (MPE), $\frac{1}{2}g\{\overline{\rho\rho}\}/\rho_\infty|\Gamma|$.

This can be seen in figure 10b, which documents the variation of the terms in the integrated mean-kinetic-energy transport equation:

$$\frac{\mathrm{d}\{K_{\alpha\alpha}\}}{\mathrm{d}t} = -\{P_{\alpha\alpha jj}\} - \{D_{\alpha\alpha jj}\} + \{B_{\alpha\alpha}\}, \qquad \alpha = (1, 2, 3), \tag{5}$$

where

$$-P_{\alpha\alpha jj} = \overline{u'_\alpha u'_j}\,\frac{\partial \overline{u}_\alpha}{\partial x_j}$$

is the mean-to-turbulence transfer term (i.e. the negative rate of TKE production),

$$D_{\alpha\alpha jj} = \nu\frac{\partial \overline{u}_\alpha}{\partial x_j}\frac{\partial \overline{u}_\alpha}{\partial x_j}$$

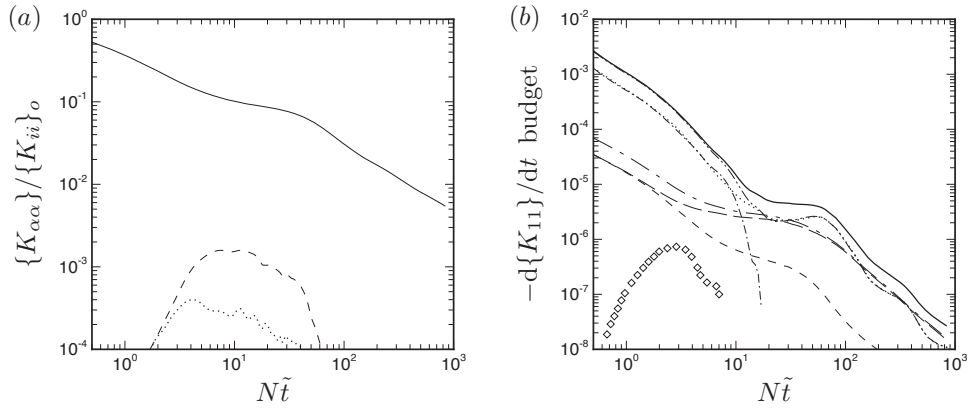

Figure 10. (*a*) Components of integrated mean kinetic energy $\{K_{\alpha\alpha}\} = \{\frac{1}{2}\overline{u}_\alpha\overline{u}_\alpha\}$ (no sum on α): ———, $\{K_{11}\}$; – – – –, $\{K_{22}\}$; ·····, $\{K_{33}\}$. Values normalized by MKE at $Nt = 0$, $\{K_{ii}\}_o = \{K_{11}\}_o + \{K_{22}\}_o + \{K_{33}\}_o$. (*b*) Terms in the budget of the streamwise mean kinetic energy $\{K_{11}\}$: – – – –, $-\{D_{1122}\} = -\{\nu(\partial\overline{u}/\partial y)^2\}$; ——— —, $-\{D_{1133}\} = -\{\nu(\partial\overline{u}/\partial z)^2\}$; ——– ——, $-\{D_{1122}\} - \{D_{1133}\}$; ·····, $-\{P_{1122}\} = \{\overline{u'v'}\,\partial\overline{u}/\partial y\}$; ——·——, $-\{P_{1133}\} = \{\overline{u'w'}\,\partial\overline{u}/\partial z\}$; ——··——, $-\{P_{1122}\} - \{P_{1133}\}$; ———, $-\{D_{1122}\} - \{D_{1133}\} - \{P_{1122}\} - \{P_{1133}\}$; $\diamond$, $\{B_{33}\} = -g\{\overline{\rho}\,\overline{w}\}/\rho_\infty$. Data for $-g\{\overline{\rho}\,\overline{w}\}/\rho_\infty$ for $N\tilde{t} > 8$ and $-\{P_{1133}\}$ for $N\tilde{t} > 18$ (when both quantities are less than 10^{-7}) not included due to excessive statistical scatter. Budget terms given in units of $U_r^3 L_r$.

is the mean dissipation rate, and

$$B_{\alpha\alpha} = -g\overline{u}_\alpha\overline{\rho}\,\delta_{\alpha 3}/\rho_\infty$$

is the mean buoyancy transfer (which appears with opposite sign in the transport equation for the mean potential energy $\frac{1}{2}g\overline{\rho}\,\overline{\rho}/\rho_\infty|\Gamma|$). Note that the integral of both the advection $A_{\alpha\alpha jj} = -\overline{u}_j\partial K_\alpha/\partial x_j$ and flux-divergence/transfer $T_{\alpha\alpha jj} = -\partial\overline{u}_\alpha\overline{u'_\alpha u'_j}/\partial x_j + \nu\,\partial[\overline{u}_\alpha\partial\overline{u}_\alpha/\partial x_j]/\partial x_j$ terms are zero, $\{A_{\alpha\alpha jj}\} = \{T_{\alpha\alpha jj}\} = 0$. It will be useful to distinguish between mean stratification effects associated with the vertical and lateral gradients. For the present flow, for which $\partial\overline{(\ )}/\partial x_1 = \partial\overline{(\ )}/\partial x = 0$, we can write $-P_{\alpha\alpha jj} = -P_{\alpha\alpha 22} - P_{\alpha\alpha 33}$ and $D_{\alpha\alpha jj} = D_{\alpha\alpha 22} + D_{\alpha\alpha 33}$, where $-P_{\alpha\alpha 22} = \overline{u'_\alpha v'}\,\partial\overline{u}_\alpha/\partial y$, $-P_{\alpha\alpha 33} = \overline{u'_\alpha w'}\,\partial\overline{u}_\alpha/\partial z$, $D_{\alpha\alpha 22} = \nu(\partial\overline{u}_\alpha/\partial y)^2$ and $D_{\alpha\alpha 33} = \nu(\partial\overline{u}_\alpha/\partial z)^2$.

The open symbols in figure 10*b* trace the evolution of the buoyancy term. Its magnitude and sign (i.e. $\{B_{33}\} = -g\{\overline{w}\,\overline{\rho}\}/\rho_\infty < 0$) imply that the buoyancy term acts as a pure sink of MKE, and source of MPE, which is largest early in the NEQ regime, until at least $N\tilde{t} \approx 9$ (it is not shown at later times because of its statistical uncertainty, exemplified by rapid small-amplitude oscillations of both signs). There are thus no mean 're-stratification effects' associated with re-conversion of mean-potential to mean-kinetic energy (cf. [2]) for the present flow's NEQ phase. The possibility that potential energy supplies kinetic energy to the turbulence during the NEQ regime will be re-examined below.

The end of the 3D period is first evident in the mean dissipation $\{D_{1122}\}$ and $\{D_{1133}\}$, in that the mean vertical gradients enhanced by the vertical flattening of the wake overwhelm the lateral variations, thereby arresting the reduction of $\{D_{1133}\}$ (compare long- and short-dashed curves in figure 10*b*). Because the dissipation terms are much smaller than the MKE-to-TKE transfer terms, their effect on the net $\mathrm{d}\{K_{11}\}/\mathrm{d}t$ is not as pronounced as that caused by the precipitous fall in magnitude of the vertical component $\{-P_{1133}\}$, and the recovery (and eventual reversal in slope) of the lateral component $\{-P_{1122}\}$, that begin

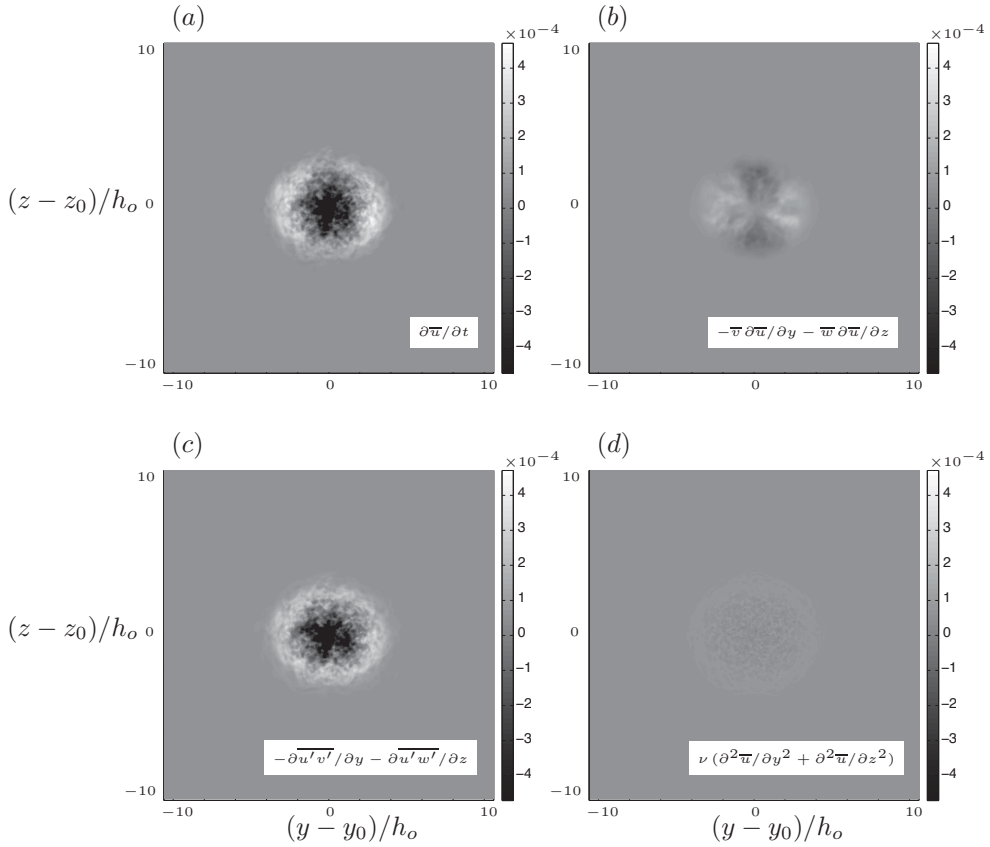

Figure 11. Terms in the mean streamwise momentum budget at $N\tilde{t} = 2.5$: (a) rate of change $\partial\overline{u}/\partial t$; (b) advection $-\overline{v}\,\partial\overline{u}/\partial y - \overline{w}\,\partial\overline{u}/\partial z$; (c) Reynolds-stress divergence $-\partial\overline{u'v'}/\partial y - \partial\overline{u'w'}/\partial z$; (d) viscous-stress divergence $\nu\,(\partial^2\overline{u}/\partial y^2 + \partial^2\overline{u}/\partial z^2)$. Terms given in units of U_r^2/L_r, where $U_r = 2.09U_{do}$ and $L_r = h_o$.

near $N\tilde{t} = 11$. Brucker & Sarkar [9] found that the rapid attenuation of P_{1133} is due to the stratification-induced collapse of the $-\overline{u'w'}$ Reynolds stress. The terms combine to yield a near-plateau of $\mathrm{d}\{K_{11}\}/\mathrm{d}t$ between $N\tilde{t} = 20$ and 50, before the flow enters its Q2D phase, when the net MKE decay is roughly split between the vertical dissipation and lateral TKE production terms.

3.4 RANS budget

In this section we examine the terms in the budget of mean streamwise momentum, and how stratification modifies their spatial structure in vertical (y-z) planes normal to the wake axis, to better understand the mechanisms responsible for the decay and spread of the mean defect during the 3D, NEQ and Q2D regimes. For the present time-dependent parallel flow the streamwise Reynolds-averaged Navier-Stokes (RANS) equation can be written

$$\frac{\partial\overline{u}}{\partial t} = \underbrace{\left(-\overline{v}\frac{\partial\overline{u}}{\partial y} - \overline{w}\frac{\partial\overline{u}}{\partial z}\right)}_{\text{advection}} + \underbrace{\left(-\frac{\partial\overline{u'v'}}{\partial y} - \frac{\partial\overline{u'w'}}{\partial z}\right)}_{\text{Reynolds-stress divergence}} + \underbrace{\nu\left(\frac{\partial^2\overline{u}}{\partial y^2} + \frac{\partial^2\overline{u}}{\partial z^2}\right)}_{\text{viscous-stress divergence}} . \quad (6)$$

During the 3D phase, the reduction in U_d and increase in the wake height and width

– i.e. the negative $\partial\overline{u}/\partial t$ near the centerline and the positive $\partial\overline{u}/\partial t$ at the wake edge – is driven by the divergence of the Reynolds stress, $-\partial\overline{u'v'}/\partial y - \partial\overline{u'w'}/\partial z$. This can be inferred from figure 11, which shows the cross-wake plane distribution of $\partial\overline{u}/\partial t$ and how the advection, turbulence and viscous terms contribute to it at $N\tilde{t} = 2.5$. At this time, the axisymmetric/3D nature of the flow has been slightly altered by the buoyancy, as the flow moves towards the NEQ regime. Although the relative strengths of the vertical and lateral components of the Reynolds-stress divergence remain comparable at the edges of the wake, the flattening and widening of the region of wake turbulence caused by the buoyant forcing is apparent (figure 11*c*). The reduced rate of vertical spreading is due to vertical advection, with $-\overline{w}\,\partial\overline{u}/\partial z < 0$ above and below the centerline (dark regions in figure 11*b*), while the lateral spreading is enhanced by the corresponding advection term, in that $-\overline{v}\,\partial\overline{u}/\partial y > 0$ at the left and right of the defect (light regions in figure 11*b*).

Within the NEQ regime the story is more complex. Figure 12*a* shows that at $N\tilde{t} = 18$, when $\mathrm{d}h_z/\mathrm{d}t \approx \mathrm{d}r_z^*/\mathrm{d}t \approx 0$, the regions at the top and bottom of the wake contain negligible $\partial\overline{u}/\partial t$, while $\overline{u}$ continues to grow at the sides. Significant internal wave activity, in the $\kappa_x = 0$ (i.e. streamwise mean) mode, is generated by the wake, revealed by the vertical mean momentum flux divergence, $-\partial\overline{u}\,\overline{w}/\partial z$ (figure 12*b*). However, the waves do not make a meaningful contribution to the net momentum (or the kinetic energy), since $-\partial\overline{u}\,\overline{w}/\partial z - \partial\overline{u}\,\overline{v}/\partial y \equiv -\overline{w}\partial\overline{u}/\partial z - \overline{v}\partial\overline{u}/\partial y$ is nearly identically zero outside the wake (figures 12*c* and *d*). The (slower, compared to 3D) rate of decrease of $U_d(t)$ is now driven by lateral Reynolds-stress divergence $-\partial\overline{u'v'}/\partial y$ and vertical advection $-\overline{w}\partial\overline{u}/\partial z$, while the lateral component $-\overline{v}\partial\overline{u}/\partial z$ retards the lateral spreading near the centerline plane but increases it further above and below (figures 12*d*). The Reynolds stresses, especially the vertical component $-\overline{u'w'}$, are profoundly affected by the buoyancy (which drives $w' \to 0$; see figure 15*b*), such that the importance of their divergence has been reduced to levels comparable to that of the vertical viscous stresses. (Contrast figures 12*e*, *f* and *g*). That viscous effects are important within the NEQ regime was illustrated by the difference in the defect histories for the primary simulation and Case R1500 (figure 7). The lateral advection and the vertical viscous terms (which tend to mirror and counteract each other) reveal a 'flattened-X' pattern in the mean velocity that is not apparent in the vertical $\overline{u}(z, y_c)$ and lateral $\overline{u}(z_c, y)$ profiles in figure 9. The lateral viscous-stress divergence (not shown) remains negligible.

The difference between the $\partial\overline{u}\,\overline{w}/\partial z$ contours in figures 12*b* ($N\tilde{t} = 18$) and 13*b* ($N\tilde{t} = 82$) displays the tendency for the strength of the internal waves to fade as the flow passes from the NEQ to Q2D regime. Once the wake enters the Q2D phase, the core deceleration is dominated by the lateral Reynolds-stress divergence, and to a lesser extent by the vertical advection and vertical viscous-stress terms. This can be seen in figures 13*e*, *c* and *f*, respectively. The vertical Reynolds-stress $-\partial\overline{u'w'}/\partial z$ and lateral viscous-stress $\nu\,\partial^2\overline{u}/\partial y^2$ terms are now negligible. We also note that the multi-layered structure first seen in the instantaneous vorticity contours earlier in the NEQ range, at $N\tilde{t} \approx 20$ (figure 5), has now matured to the point it affects the RANS budget, leaving its signature in the terms involving spatial gradients of the mean velocity, such as $-\overline{v}\partial\overline{u}/\partial y$ (figure 13*d*). At the top and bottom edges of the wake, the vertical viscous-stress divergence is now solely responsible for the small net positive $\partial\overline{u}/\partial t$ here – a fact foreshadowed by the $t^{1/2}$ growth of the mean height observed in figure 7*c*. In contrast, the (faster) lateral spreading is due to the lateral advection (figure 13*d*) and especially the lateral Reynolds-stress term (figure 13*e*).

As time passes, the importance of the $-\partial\overline{u'v'}/\partial y$ and $\nu\,\partial^2\overline{u}/\partial z^2$ terms continues to grow relative to the other ones, until they are the only significant contributors to the RANS budget (cf. Meunier *et al.* [3]). At $N\tilde{t} = 586$ (figure 14), both decelerate the core region by about the same amount, but have much different effects on the spreading of the defect: the mean acceleration at the top and bottom of the defect caused by the viscous diffusion is much weaker than that produced at the sides by the lateral divergence of the $-\overline{u'v'}$ Reynolds

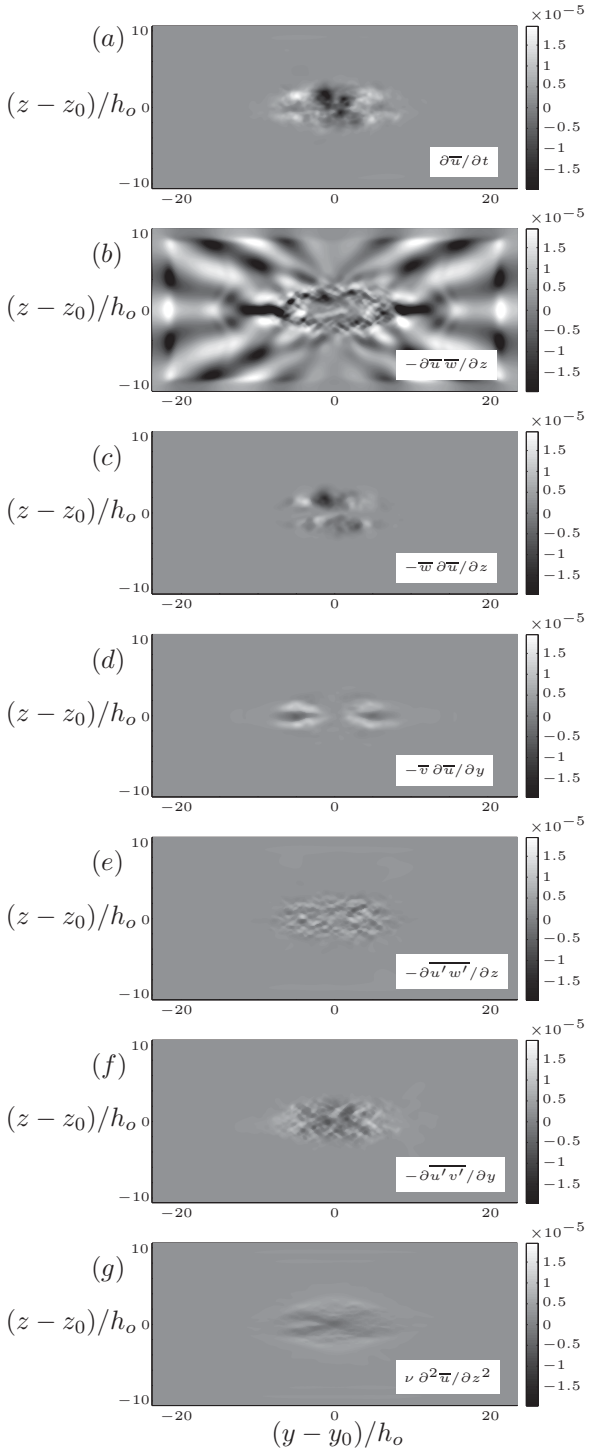

Figure 12. Terms in mean streamwise momentum budget at $N\tilde{t} = 18$ (NEQ regime): (a) rate of change $\partial\overline{u}/\partial t$; (b) $-\partial\overline{u}\,\overline{w}/\partial z$; (c) vertical advection $-\overline{w}\,\partial\overline{u}/\partial z$; (d) lateral advection $-\overline{v}\,\partial\overline{u}/\partial y$; (e) vertical Reynolds-stress divergence $-\partial\overline{u'w'}/\partial z$; (f) lateral Reynolds-stress divergence $-\partial\overline{u'v'}/\partial y$; (g) vertical viscous-stress divergence $\nu\,\partial^2\overline{u}/\partial z^2$. Lateral viscous-stress divergence $\nu\,\partial^2\overline{u}/\partial y^2$ is negligible compared to terms shown. Terms given in units of U_r^2/L_r, where $U_r = 2.09U_{do}$ and $L_r = h_o$.

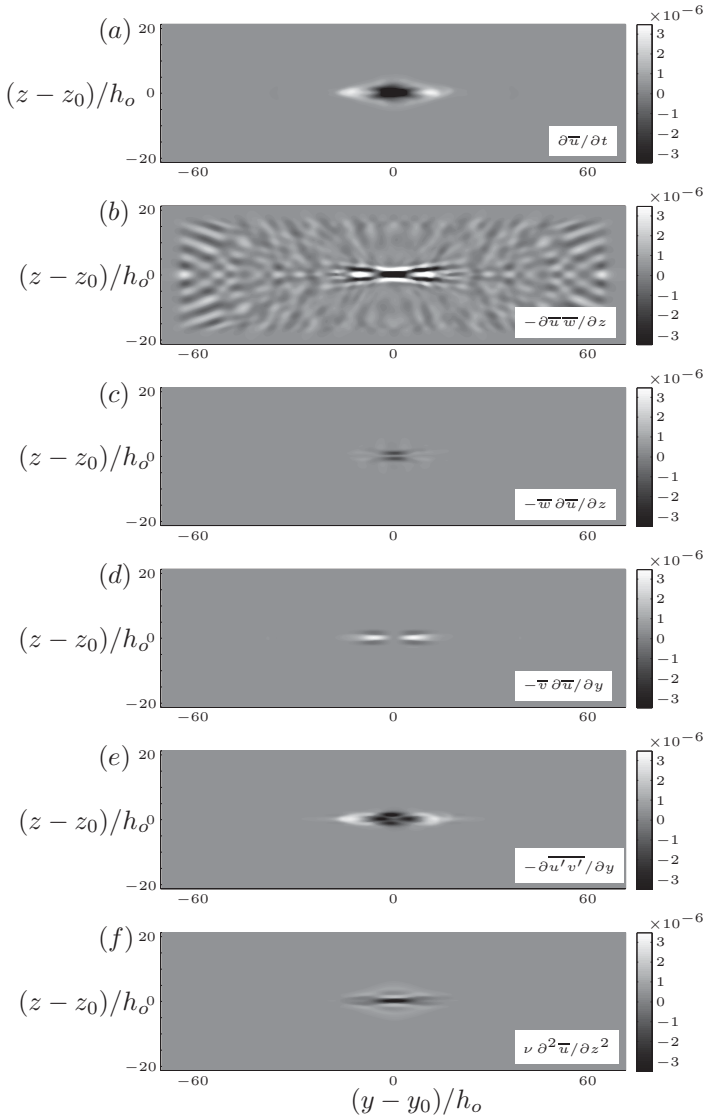

Figure 13. Terms in mean streamwise momentum budget at $N\tilde{t} = 82$ (Q2D regime): (a) rate of change $\partial\overline{u}/\partial t$; (b) $-\partial\overline{u}\,\overline{w}/\partial z$; (c) vertical advection $-\overline{w}\,\partial\overline{u}/\partial z$; (d) lateral advection $-\overline{v}\,\partial\overline{u}/\partial y$; (e) lateral Reynolds-stress divergence $-\partial\overline{u'v'}/\partial y$; (f) vertical viscous-stress divergence $\nu\,\partial^2\overline{u}/\partial z^2$. Vertical Reynolds-stress divergence $-\partial\overline{u'w'}/\partial z$ and lateral viscous-stress divergence $\nu\,\partial^2\overline{u}/\partial y^2$ are negligible compared to terms shown. Terms given in units of U_r^2/L_r, where $U_r = 2.09U_{do}$ and $L_r = h_o$.

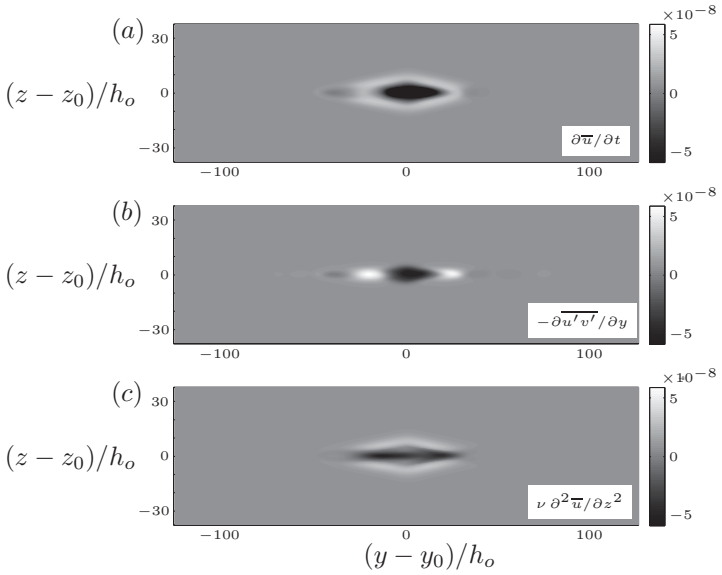

Figure 14. Terms in mean streamwise momentum budget at $N\tilde{t} = 586$ (late Q2D regime): (a) rate of change $\partial\overline{u}/\partial t$; ($b$) lateral Reynolds-stress divergence $-\partial\overline{u'v'}/\partial y$; ($c$) vertical viscous-stress divergence $\nu\,\partial^2\overline{u}/\partial z^2$. Vertical mean-flow momentum divergence $-\partial\overline{u}\,\overline{w}/\partial z$, advection $-\overline{v}\,\partial\overline{u}/\partial y - \overline{w}\,\partial\overline{u}/\partial z$, vertical Reynolds-stress divergence $-\partial\overline{u'w'}/\partial z$ and lateral viscous-stress divergence $\nu\,\partial^2\overline{u}/\partial y^2$ are negligible compared to terms shown. Terms given in units of U_r^2/L_r, where $U_r = 2.09U_{do}$ and $L_r = h_o$.

stress, induced by the pancake-eddy turbulence (cf. figure 6). (The lateral asymmetry of the $-\partial\overline{u'v'}/\partial y$ contours in figure 14b is a statistical anomaly, due to the relatively small number of eddy structures included in the streamwise average at this time.) The decoupling of the viscous/vertical and turbulent/lateral mixing mechanisms during the late-Q2D regime is consistent with the disparate rates of vertical and lateral spreading observed in figures 7(c, d), with β_z larger than β_y for $N\tilde{t} > 100$, and the earlier observation that the growth of h_z is a purely viscous phenomenon during this time.

3.5 Turbulence kinetic energy history and budget

Figure 15a summarizes the manner in which stratification alters the cross-wake-averaged potential and kinetic energy of the turbulence, $\frac{1}{2}g\langle\overline{\rho'\rho'}\rangle/\rho_\infty|\Gamma|$ (symbols) and $\langle k\rangle = \frac{1}{2}\langle\overline{u_i'u_i'}\rangle$ (lines), respectively. (Recall the cross-wake average is over regions where $\overline{u} \geq 0.05\,U_d$.)

The density fluctuations are largest early in the NEQ regime, when buoyancy most strongly affects the flow, but contain negligible energy compared to that in the velocity fluctuations throughout the wake's lifetime (note the factor of 10^3 multiplying the potential energy in figure 15a).

The present flow, with its much larger initial Froude number ($F_\infty \approx 130$), does not contain the buoyancy-induced temporal oscillations of TKE observed at early times in Dommermuth *et al.*'s [8] $F_\infty = 4$ LES and Brucker & Sarkar's [9] $F_\infty = 8$ DNS, for which $\mathrm{d}k/\mathrm{d}t$ first becomes positive near $N\tilde{t} = 5.5$ for the former and $N\tilde{t} = 2.3$ for the latter (see figure 21 regarding values of the virtual origin $N\tilde{t}_{vo}$ used for those simulations). Those oscillations, which are damped more slowly in the lower F_∞ flow, are indicative of transfer back and forth between the potential and kinetic energy of the turbulence, associated with changes in sign of the TKE-to-turbulence potential energy (TPE) exchange term, $\mathcal{B}_{\mathsf{tke}} = -g\overline{\rho'w'}/\rho_\infty$

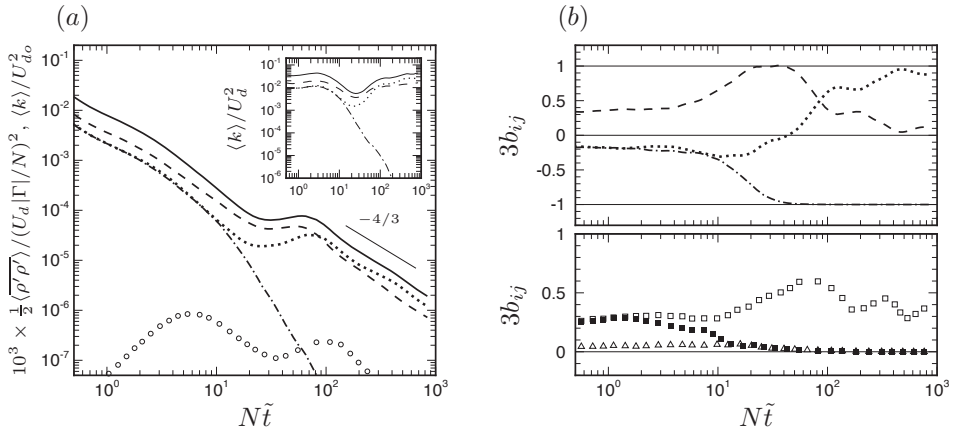

Figure 15. (a) Cross-wake-averaged turbulence potential and kinetic energy histories: ○, $\frac{1}{2}\overline{\langle \rho'\rho' \rangle}$; ——, $\langle k \rangle$; – – – –, $\frac{1}{2}\overline{\langle u'u' \rangle}$; ·····, $\frac{1}{2}\overline{\langle v'v' \rangle}$; —·—·—, $\frac{1}{2}\overline{\langle w'w' \rangle}$. Inset plot shows components scaled by local U_d. (b) Reynolds stress anistropy $b_{ij} = \langle |\overline{u_i'u_j'}| \rangle / 2\langle k \rangle - \delta_{ij}/3$ histories: – – – –, b_{11}; ·····, b_{22}; —·—·—, b_{33}; □, b_{12}; ■, b_{13}; △, b_{23}.

(Brucker & Sarkar mention, but do not quantify, 'large values of the buoyancy flux at early time'). For the present flow, $\mathcal{B}_{\mathsf{tke}}$ always acts as a net sink of TKE (figure 3b) despite the monotonic decrease with time of the local mean Froude number F_d (figure 1a, b).

Instead of increasing towards the beginning of the NEQ regime, here the TKE increases for $30 < N\tilde{t} < 70$, i.e. during the NEQ-to-Q2D transition defined by the U_d history (figure 7b). The reasons for this increase, which are unrelated to the TPE-to-TKE transfer via $\mathcal{B}_{\mathsf{tke}}$, will soon be clear.

The difference between the rates of decay of the three velocity fluctuations, as well as the non-constant variation of $\langle k \rangle / U_d^2$ for $N\tilde{t} > 4$ (solid curve in figure 15a inset), demonstrate the anisotropy introduced by the stratification, and how it breaks the early-time axisymmetry, leading to a flow for which the relationship between the magnitude of the velocity fluctuations and the maximum mean defect continues to evolve throughout the NEQ and Q2D regimes. Of the three components, the streamwise TKE $\frac{1}{2}\overline{\langle u'u' \rangle}$ (dashed curve) exhibits the least variation with respect to the local U_d^2, but even so varies significantly (by over a factor of five) as the wake regimes come and go. For $N\tilde{t} > 150$, when the TKE is reasonably approximated by a $t^{-4/3}$ power law, k decays more slowly than U_d^2 does, such that (assuming $U_d \sim t^{-0.85}$ in the Q2D range) $k/U_d^2 \sim t^{+0.37}$ (figure 15a inset plot).

The disparate effect of the stratification upon the three velocity-fluctuation components, and thus on the structure of the Reynolds-stress tensor, can also be seen in figure 15b. These Reynolds-stress-anisotropy histories show that the velocity fluctuations first deviate from axisymmetric-decay behavior (i.e. $\overline{v'v'} \approx \overline{w'w'}$ and $\overline{u'v'} \approx \overline{u'w'}$) near $N\tilde{t} = 2$, the time at which the mean-defect height and width begin to differ from each other (figure 7c, d). Thereafter, the vertical component falls monotonically, first slowly then precipitously, such that $\overline{w'w'}$ and both $\overline{u'w'}$ and $\overline{v'w'}$ are negligible for $N\tilde{t} > 40$ (cf. Spedding [12] and Diamessis *et al.* [2]). The absence of vertical velocity means that buoyancy can no longer directly cause a transfer between the turbulence potential and kinetic energies.

The streamwise normal stress $\overline{u'u'}$ becomes a larger and larger fraction of the $2k = \overline{u'u'} + \overline{v'v'} + \overline{w'w'}$ total until the flow is well within the NEQ regime, when $\mathrm{d}k/\mathrm{d}t$ becomes positive, near $N\tilde{t} \approx 30$. Afterwards, the normal component $\overline{v'v'}$ increases faster than $\overline{u'u'}$, and $\overline{u'v'}$ is the only significant shear stress. The dominance of $\overline{u'v'}$ corresponds to that of the $P_{1122} = -\overline{u'v'}\partial\overline{u}/\partial y$ production term; recall the importance of $-\{P_{1122}\}$ in the $\{K_{11}\}$

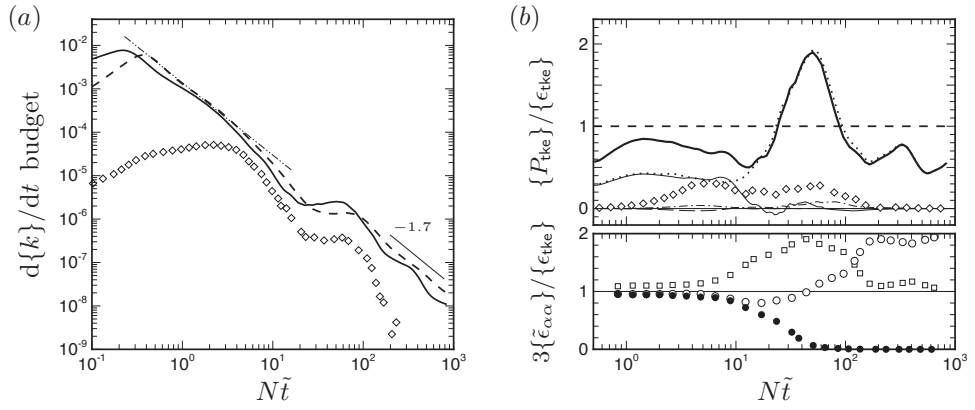

Figure 16. Terms in the budget of integrated TKE $\{k\}$: ———, rate of production $\{P_{\mathsf{tke}}\}$; – – – –, rate of dissipation $\{\epsilon_{\mathsf{tke}}\}$; ◇, (minus) rate of buoyancy transfer $-\{B_{\mathsf{tke}}\}$; ····· (in b only), $\{P_{1122}\}$; thin-solid (———) (in b only), $\{P_{1133}\}$; ——·—— (in b only), $\{P_{2222}\}$; ——– – ——– (in b only), $\{P_{3333}\}$; □ (in b only), $\{\tilde{\epsilon}_{11}\}$; ○ (in b only), $\{\tilde{\epsilon}_{22}\}$; • (in b only), $\{\tilde{\epsilon}_{33}\}$; ——··—— (in a only), $A_\epsilon(N\tilde{t})^{-5/3} = A_\epsilon(Nt - Nt_{vo})^{-5/3}$, with $(A_\epsilon, Nt_{vo}) = (0.00138, 0.645)$. Production terms not shown are either zero because of homogeneity ($\{P_{1111}\} = \{P_{2211}\} = \{P_{3311}\} \equiv 0$) or negligible ($\{P_{2233}\} \approx \{P_{3322}\} \approx 0$). Components of dissipation rate $\tilde{\epsilon}_{\alpha\alpha} = \nu\overline{(\partial u'_\alpha/\partial x_j)(\partial u'_\alpha/\partial x_j)}$ (no sum on α), where $\tilde{\epsilon}_{ii} = \epsilon_{\mathsf{tke}} - \nu\partial^2\overline{u'_i u'_j}/\partial x_i \partial x_j$, and $\epsilon_{\mathsf{tke}} = 2\nu\overline{s'_{ij}s'_{ij}}$. Terms in ($a$) given in units of $U_r^3 L_r$, in (b) as fraction of local $\{\epsilon_{\mathsf{tke}}\}$.

budget and see below. During the $N\tilde{t} > 70$ phase of the Q2D regime, when $\mathrm{d}k/\mathrm{d}t$ is again negative (and the flow is dominated by pancake-eddy structures), the lateral fluctuations have more energy than the streamwise fluctuations do, with $\langle\overline{v'v'}\rangle/\langle\overline{u'u'}\rangle \to 2$ for $N\tilde{t} > 400$.

We now consider the transport equation for the TKE k,

$$\frac{\partial k}{\partial t} = \mathcal{A}_{\mathsf{tke}} + \mathcal{P}_{\mathsf{tke}} + \mathcal{F}_{\mathsf{tke}} + \mathcal{B}_{\mathsf{tke}} - \epsilon_{\mathsf{tke}} + \mathcal{W}_{\mathsf{tke}}, \tag{7}$$

where the rates of change due to advection $\mathcal{A}_{\mathsf{tke}}$, production $\mathcal{P}_{\mathsf{tke}}$, flux divergence $\mathcal{F}_{\mathsf{tke}}$, buoyancy transport $\mathcal{B}_{\mathsf{tke}}$ and dissipation ϵ_{tke} are, respectively, $\mathcal{A}_{\mathsf{tke}} = -\overline{u}_j\partial k/\partial x_j$, $\mathcal{P}_{\mathsf{tke}} = P_{iijj} = -\overline{u'_i u'_j}\partial\overline{u}_i/\partial x_j$, $\mathcal{F}_{\mathsf{tke}} = \partial f_j/\partial x_j$, with $f_j = -\frac{1}{2}\overline{u'_j u'_i u'_i} - \overline{u'_j p'}/\rho_\infty + \nu\partial\overline{u'_i u'_j}/\partial x_i + \nu\partial k/\partial x_j$, and $\mathcal{B}_{\mathsf{tke}} = -g\overline{\rho' u'_i}\delta_{i3}/\rho_\infty$ and $\epsilon_{\mathsf{tke}} = 2\nu\overline{s'_{ij}s'_{ij}}$, with $s'_{ij} = \frac{1}{2}(\partial u'_i/\partial x_j + \partial u'_j/\partial x_i)$. For the flow at hand, these reduce to $\mathcal{A}_{\mathsf{tke}} = -\overline{v}\partial k/\partial y - \overline{w}\partial k/\partial z$, $\mathcal{P}_{\mathsf{tke}} = P_{ii22} + P_{ii33}$, $\mathcal{F}_{\mathsf{tke}} = \partial[-\frac{1}{2}\overline{v' u'_i u'_i} - \overline{v'p'}/\rho_\infty + \nu\partial\overline{v'v'}/\partial y + \nu\partial\overline{v'w'}/\partial z + \nu\partial k/\partial y]/\partial y + \partial[-\frac{1}{2}\overline{w' u'_i u'_i} - \overline{w'p'}/\rho_\infty + \nu\partial\overline{v'w'}/\partial y + \nu\partial\overline{w'w'}/\partial z + \nu\partial k/\partial z]/\partial z$ and $\mathcal{B}_{\mathsf{tke}} = -g\overline{\rho'w'}/\rho_\infty$. The work done by the fringe forcing F_i in (1) is $\mathcal{W}_{\mathsf{tke}} = \overline{u'_i F_i}$ ($i = 1, 2, 3$).

We begin by examining the cross-plane-area-integrated histories of the terms in (7), shown in figure 16. (This information was presented in a different format in figure 3b; it is repeated here to highlight the relative importance of individual budget terms.) The cross-plane averages used in figure 15 can be approximated from the cross-plane integrations used in figure 16 by dividing the latter by the cross-sectional area of the mean defect, such that e.g. $\langle k\rangle \approx \{k\}/4\pi h_y h_z$. Since the advection and flux-divergence terms integrate to zero, figure 16 reveals the contributions of the pure source $\mathcal{P}_{\mathsf{tke}}$, sink ϵ_{tke} and TKE-TPE transfer $\mathcal{B}_{\mathsf{tke}}$. The cross-plane variation of these terms, and $\mathcal{A}_{\mathsf{tke}}(y,z)$ and $\mathcal{F}_{\mathsf{tke}}(y,z)$, will be investigated below.

For the present high-F_∞ flow, the fringe-work contribution $\{\mathcal{W}_{\mathsf{tke}}\}$ to the TKE balance is negligible (recall that the production, dissipation and buoyancy sum shown in figure 3b is

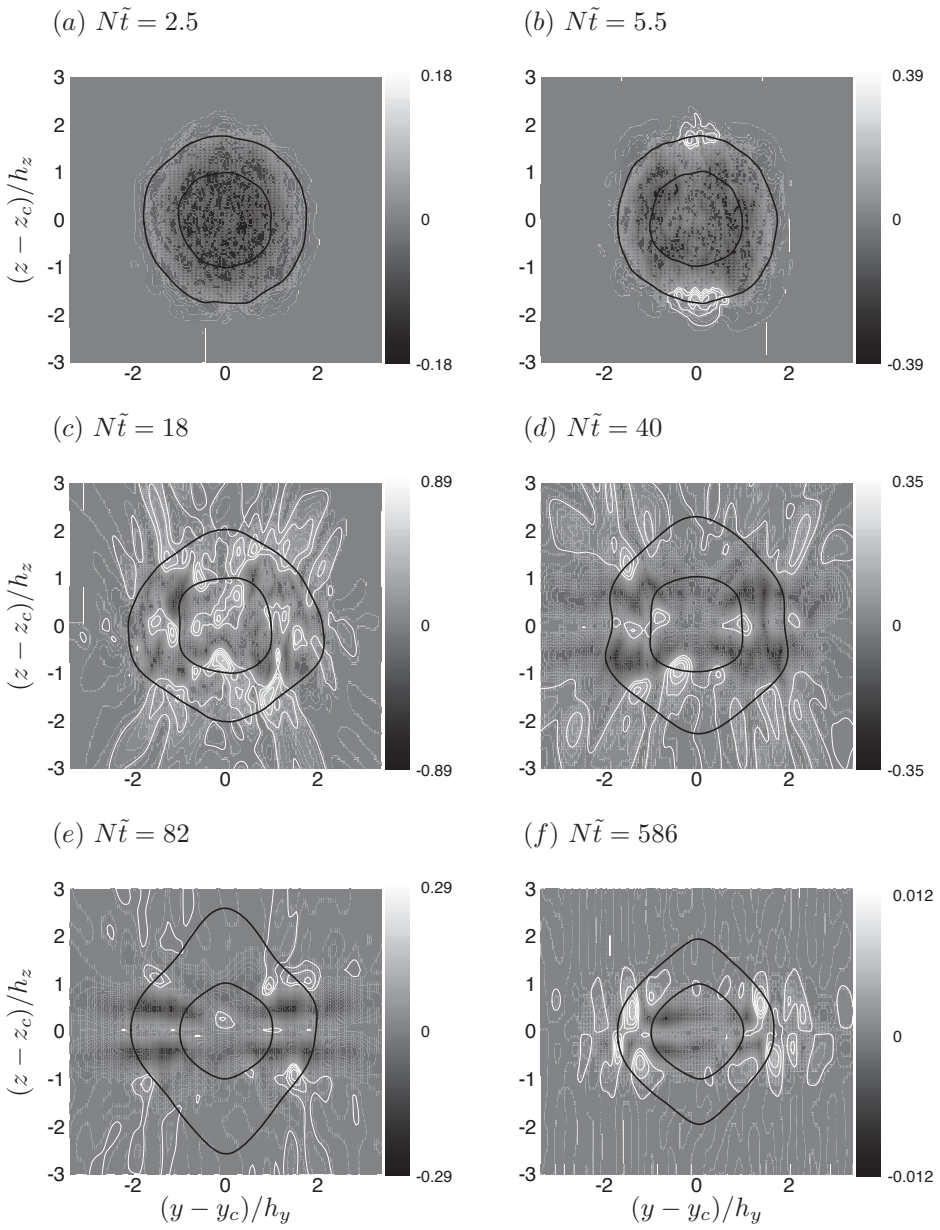

Figure 17. Contours of buoyancy transfer $\mathcal{B}_{\mathsf{tke}}$ as a fraction of $(\epsilon_{\mathsf{tke}})_{\max}$, the local maximum ϵ_{tke} from figure 20, at: (*a*) $N\tilde{t} = 2.5$, (*b*) $N\tilde{t} = 5.5$, (*c*) $N\tilde{t} = 18$, (*d*) $N\tilde{t} = 40$, (*e*) $N\tilde{t} = 82$ and (*f*) $N\tilde{t} = 586$. Minimum (darkest) contour level -C_{lim} corresponds to the most negative $\mathcal{B}_{\mathsf{tke}}/(\epsilon_{\mathsf{tke}})_{\max}$ at each time. White solid-line contours indicate five levels of positive $\mathcal{B}_{\mathsf{tke}}/(\epsilon_{\mathsf{tke}})_{\max}$, over range $+0.01|C_{\mathrm{lim}}| \leq \mathcal{B}_{\mathsf{tke}}/(\epsilon_{\mathsf{tke}})_{\max} \leq [\mathcal{B}_{\mathsf{tke}}/(\epsilon_{\mathsf{tke}})_{\max}]_{\max}$, where $[\mathcal{B}_{\mathsf{tke}}/(\epsilon_{\mathsf{tke}})_{\max}]_{\max}$ is maximum $\mathcal{B}_{\mathsf{tke}}/(\epsilon_{\mathsf{tke}})_{\max}$, which at $N\tilde{t} = 2.5$, 5.5, 18, 40, 82 and 586 is respectively +0.0007, +0.085, +0.37, +0.14, +0.06 and +0.005. Black solid-line contours correspond to $\overline{u} = 0.05U_d$ and $0.5U_d$.

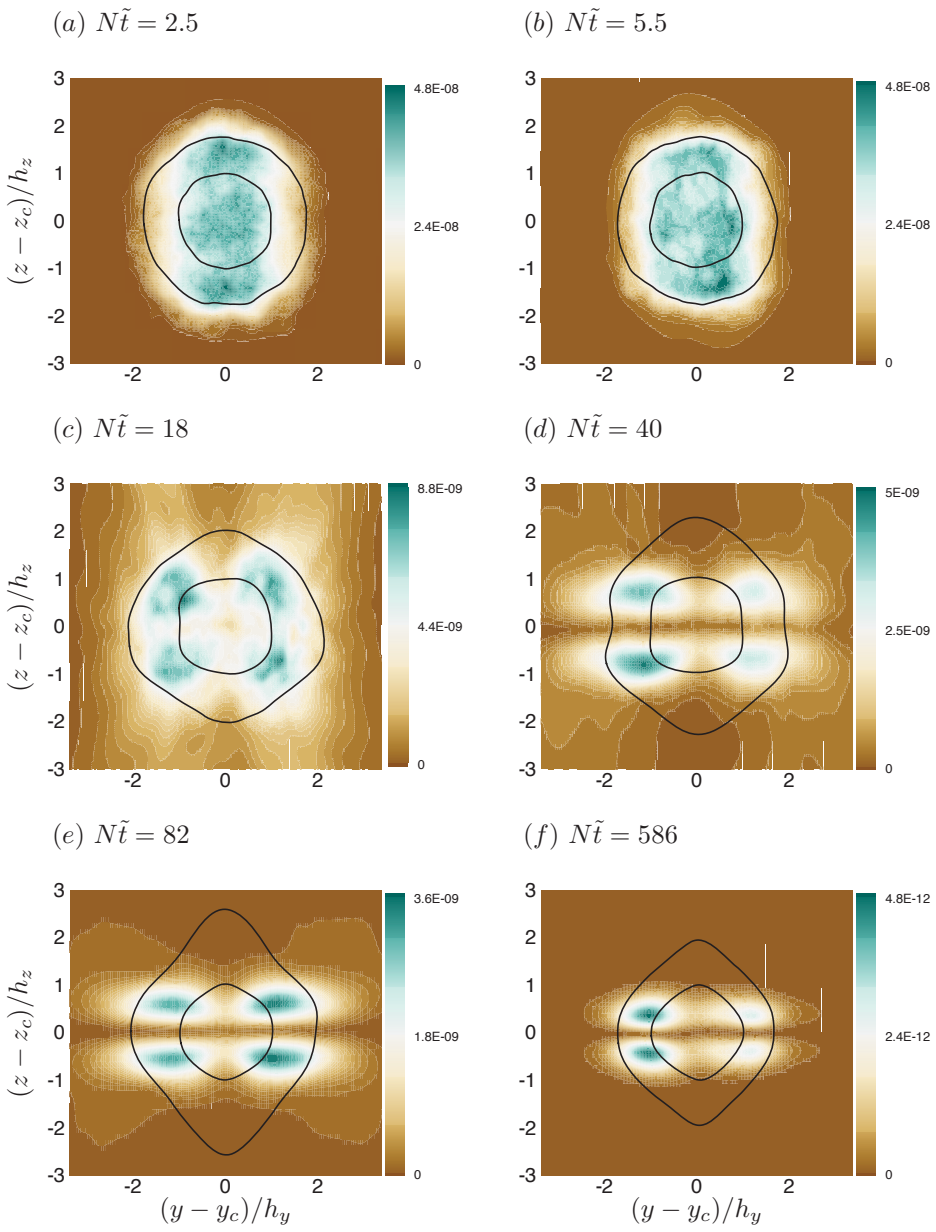

Figure 18. Contours of density-fluctuation variance $\overline{\rho'\rho'}$ at: (*a*) $N\tilde{t} = 2.5$, (*b*) $N\tilde{t} = 5.5$, (*c*) $N\tilde{t} = 18$, (*d*) $N\tilde{t} = 40$, (*e*) $N\tilde{t} = 82$ and (*f*) $N\tilde{t} = 586$. Values given in units of $(\rho_\infty U_r^2/gL_r)^2$. Solid-line contours correspond to $\overline{u} = 0.05U_d$ and $0.5U_d$.

sufficient to provide an excellent representation of the $\mathrm{d}\{k\}/\mathrm{d}t$ history, for $0 \leq Nt < 840$.) The net buoyancy transfer is also much smaller than the production and dissipation, but is not negligible, with $-\{\mathcal{B}_{\mathsf{tke}}\}$ reaching a maximum of about 30% of the integrated dissipation $\{\epsilon_{\mathsf{tke}}\}$ from early in the NEQ regime ($N\tilde{t} \approx 5$) and remaining fixed near this ratio until $N\tilde{t} \approx 70$ (figure 16*b*), after which $-\{\mathcal{B}_{\mathsf{tke}}\}$ is a monotonically decreasing fraction of $\{\epsilon_{\mathsf{tke}}\}$ until it becomes negligible after $N\tilde{t} \approx 150$. Between $N\tilde{t} \approx 25$ and 70, all three non-negligible terms are roughly constant in absolute terms, with $\mathrm{d}\{\epsilon_{\mathsf{tke}}\}/\mathrm{d}t$ and $\mathrm{d}\{\mathcal{B}_{\mathsf{tke}}\}/\mathrm{d}t$ approximately zero and $\mathrm{d}\{\mathcal{P}_{\mathsf{tke}}\}/\mathrm{d}t$ increasing slightly. Spedding [12] found a similar NEQ plauteau in the total dissipation $\epsilon_{\mathsf{tke}} + D_{iijj}$ in his high-F_∞ experiments, which he attributed to 'vertical shear taking over'. We have already observed that the global/integrated buoyancy transfer $\{\mathcal{B}_{\mathsf{tke}}\}$ acts as a pure sink throughout the lifetime of the present flow (figure 3*b*). At times, however, there are local regions in which $\mathcal{B}_{\mathsf{tke}}$ is positive, where the potential energy of the turbulence is converted to kinetic energy. During the early NEQ phase, these tend to be concentrated just above and below the wake (see white-line contours in figure 17*b*), while later they are more diffuse and disorganized, although still occurring mostly outside the wake core (figure 17*c*-*e*). Much later, in the viscous-dominated Q2D regime, when $\{\mathcal{B}_{\mathsf{tke}}\}/\{\epsilon_{\mathsf{tke}}\} \to 0$, positive $\mathcal{B}_{\mathsf{tke}}$ tends to lie in the non-vortical regions to the left and right sides of the wake (figure 17*f*). The relationship between $\mathcal{B}_{\mathsf{tke}}$ and the density fluctuations $\overline{\rho'\rho'}$ can be inferred by comparing figures 17 and 18. The regions of maximum negative $\mathcal{B}_{\mathsf{tke}}$ are in general highly correlated with those of maximum $|\rho'|$, although the departure from axisymmetry associated with the beginning of the NEQ regime is more apparent in the $\overline{\rho'\rho'}$ field at $N\tilde{t} = 2.5$ (figure 18*a*) than in the corresponding $\mathcal{B}_{\mathsf{tke}}$ distribution (figure 17*a*). The local $\overline{\rho'\rho'}$ maxima at $N\tilde{t} = 2.5$ at the top and bottom of the wake, near $z = \pm 1.5 h_z$, are consistent with the 'excess' TPE that later 'springs back' into TKE at these locations, by way of the positive $\mathcal{B}_{\mathsf{tke}}$ observed in figure 17*b* at $N\tilde{t} = 5.5$.

Figure 16*a* shows that the Reynolds number is large enough for the early/3D-regime evolution to satisfy the inertial scaling $\epsilon_{\mathsf{tke}} \sim k^{3/2}/h$, such that $\epsilon_{\mathsf{tke}} \sim t^{-7/3}$ and $\{\epsilon_{\mathsf{tke}}\} \sim t^{-5/3}$ (chain-double-dot curve; cf. Brucker & Sarkar [9]). For late times, $N\tilde{t} > 200$ or so, the decay of $\{\mathcal{P}_{\mathsf{tke}}\}$ and especially $\{\epsilon_{\mathsf{tke}}\}$ is reasonably well approximated by t^{-n} with $n = 1.7 \approx 5/3$. Thus, paradoxically, the TKE dissipation evolves according to the inertial scaling during both the 3D and Q2D regimes, despite their qualitatively different eddy structures (see figure20*d*).

Once the wake turbulence is fully established, the net rate of TKE dissipation is larger than that of the production $\mathcal{P}_{\mathsf{tke}}$, except for a substantial period during the NEQ regime, from $N\tilde{t} \approx 20$ to 90, when $\{\mathcal{P}_{\mathsf{tke}}\}$ is significantly larger than $\{\epsilon_{\mathsf{tke}}\}$ (and gradually increases, in absolute terms), after which it returns to its pre-NEQ behavior, with $\{\mathcal{P}_{\mathsf{tke}}\}/\{\epsilon_{\mathsf{tke}}\} < 1$ for the Q2D phase. This explains the growth of TKE during this period, mentioned above. From figure 16*b* we find that the enhanced NEQ-regime production is due solely to amplification of the $P_{1122} = -\overline{u'v'}\,\partial\overline{u}/\partial y$ component (dotted curve), since the $-\overline{u'v'}$ stress grows more rapidly than $\partial\overline{u}/\partial y$ decreases (and the fall of $\overline{u'w'}$ is more rapid than the attenuation of the decay of $\partial\overline{u}/\partial z$; see figure 16*b* and histories of the MKE dissipation components $D_{1122} = \nu(\partial\overline{u}/\partial y)^2$ and $D_{1133} = \nu(\partial\overline{u}/\partial z)^2$ in figure 10). This 'structural' alteration, represented by the decrease of $|\overline{u'w'}|$ and increase of $|\overline{u'v'}|$, was also found by Brucker & Sarkar [9] in their DNS for both towed and self-propelled cases. They concluded that stratification causes the TKE production to mainly consist of P_{1122} during this time. The present results underline the extent to which this is true, and that in fact $\mathcal{P}_{\mathsf{tke}}$ can effectively be replaced by P_{1122} for all times after $N\tilde{t} \approx 20$.

While both the present and Brucker & Sarkar simulations contain enhanced production, only here does it lead to growth of TKE (and not just reduction in the net TKE decay) during the NEQ regime. This is because of the large amount of energy radiated by internal waves between $N\tilde{t} = 25$ and 75 in Brucker & Sarkar's $F_\infty = 8$ flow, which counteracts the impact of the P_{1122} growth. The strength of the internal waves is an indication of when

the TKE growth occurs. When they are strong, at low F_∞, buoyancy leads to an early TKE increase driven by the TPE-to-TKE transfer, before the NEQ regime begins – during which the energy the waves radiate mitigates the effect of the enhanced TKE production associated with the flattened, two-layer NEQ structure, and $\mathrm{d}\{k\}/\mathrm{d}t$ is small but negative. When the waves are weak, at high F_∞, they do not attenuate the enhanced $\mathcal{P}_{\mathsf{tke}} \approx P_{1122}$, leading to net TKE growth during the NEQ regime.

Also included in figure 16*b* are histories of the three components of the integrated rate of homogeneous dissipation, $\{\tilde{\epsilon}_{ii}\} = \{\tilde{\epsilon}_{11}\} + \{\tilde{\epsilon}_{22}\} + \{\tilde{\epsilon}_{33}\}$, as a fraction of the full (actual, thermodynamic) rate of TKE dissipation $\{\epsilon_{\mathsf{tke}}\} = 2\nu\{s'_{ij}s'_{ij}\}$, where $\tilde{\epsilon}_{ii} = \nu\overline{(\partial u'_i/\partial x_j)(\partial u'_i/\partial x_j)}$. (There is very little difference between the integrated homogeneous and full/inhomogeneous dissipation for this flow, with $0.9999965 \leq \{\tilde{\epsilon}_{ii}\}/\{\epsilon_{\mathsf{tke}}\} \leq 1.0012$ for all times considered.) Examining $\tilde{\epsilon}_{\alpha\alpha}$ for $\alpha = 1, 2, 3$ allows us to assess the interplay between the rates of production and dissipation of the individual normal-stress components $\overline{u'_\alpha u'_\alpha}$. (Other dissipation decompositions have been utilized by Spedding [12] and Brucker & Sarkar [9]; see also Itsweire *et al.* [32].)

The vertical component $\{\tilde{\epsilon}_{33}\} \sim \{(\partial w'/\partial x)^2\} + \{(\partial w'/\partial y)^2\} + \{(\partial w'/\partial z)^2\}$ falls monotonically as w' does, with $\mathrm{d}\{\tilde{\epsilon}_{33}\}/\mathrm{d}t$ becoming negative from $N\tilde{t} \approx 7$ until $N\tilde{t} > 50$, when $\{\tilde{\epsilon_{33}}\}$ is negligible with respect to $\{\epsilon_{\mathsf{tke}}\}$.

For the streamwise component, the increase in P_{1122} for $N\tilde{t} > 5$ is accompanied by an increase in $\{\tilde{\epsilon}_{11}\}$, such that the net effect (to which the pressure-strain correlation $\phi_{11} = \overline{p'(\partial u'/\partial x)}/\rho_\infty$ may also contribute) is to arrest the decay of $\overline{u'u'}$, such that $\mathrm{d}\{\overline{u'u'}\}/\mathrm{d}t$ first changes sign and then becomes slightly positive as the flow enters its NEQ phase (figure 15*a*). This is an example of what is often referred to as an 'extra strain' effect (Bradshaw [33]), which involves a difficult-to-model change that results from the imbalance of much larger terms of opposite sign, each of which change much more than the net imbalance. Similar behavior is found in the Q2D regime, in that as $\mathrm{d}\{\overline{u'u'}\}/\mathrm{d}t$ becomes negative again, both $\{P_{1122}\}$ and $\{\tilde{\epsilon}_{11}\}$ decrease (the latter accounting for roughly one-third of the total $\{\epsilon_{\mathsf{tke}}\}$).

The evolution of the lateral component during the 3D-to-NEQ transition is not directly affected by production (since $P_{2211} \equiv 0$ and $P_{2222} \approx P_{2233} \approx 0$). Consequently, the slight increase in $\{\overline{v'v'}\}$ between $N\tilde{t} \approx 25$ and 80 shown in figure 15*a* must be due to inter-component transfer via the pressure-strain term $\phi_{22} = \overline{p'(\partial v'/\partial y)}/\rho_\infty$, mitigated by $\{\tilde{\epsilon}_{22}\}$, which first falls slightly below $\{\epsilon_{\mathsf{tke}}\}/3$ (i.e. the isotropic value approximated by all three components before $N\tilde{t} \approx 5$), then grows to account for about 2/3 of the total.

The dissipation histories are broadly consistent with those observed in Brucker & Sarkar's [9] low-F_∞/self-propelled wake simulation, in that $\overline{(\partial u'/\partial z)^2}$ and $\overline{(\partial v'/\partial z)^2}$ (i.e. the dominant terms in $\tilde{\epsilon}_{11}$ and $\tilde{\epsilon}_{22}$, respectively) are respectively the second-largest and largest terms for $N\tilde{t} > 10$ (although the contributions of $\partial v'/\partial x$, $\partial w'/\partial x$ and $\partial w'/\partial z$ were not quantified, these are likely to be negligible). The $\{\tilde{\epsilon}_{\alpha\alpha}\}$ histories are thus also consistent with the enhanced vertical gradients associated with the flattened eddy structures of the NEQ and Q2D regimes (figures 5 and 6). We note that $\{\tilde{\epsilon}_{22}\}/\{\tilde{\epsilon}_{11}\} \approx 2$ for $N\tilde{t} > 150$ while $\langle\overline{v'v'}\rangle/\langle\overline{u'u'}\rangle > 1.7$ in the late-Q2D regime, i.e. for $N\tilde{t} > 500$ (figure 15*b*).

Terms in the TKE budget for the (essentially) unstratified axisymmetric benchmark at $N\tilde{t} = 1.2$ are illustrated in figure 19. Shown are radial profiles of the production $\mathcal{P}_{\mathsf{tke}}$, dissipation ϵ_{tke}, buoyancy transport $\mathcal{B}_{\mathsf{tke}}$ (which at this time is very small) and the flux divergence $\mathcal{F}_{\mathsf{tke}}$, which solely redistributes TKE within (and thus integrates to zero over) the y-z plane, and thus played no role in the integrated budget histories considered to this point. The importance of the flux divergence (open symbols) is indicated by the large contribution it makes to the net $\partial k/\partial t$ (solid symbols), especially to the TKE growth at the edge of the wake. The shapes of the production and dissipation profiles are the same as those found in the self-similar axisymmetric experiment of Uberoi & Freymouth [34], but here the transport increases the TKE not just at the edge of the wake (as it does in the experiment) but also near the centerline. (The difference is perhaps a consequence of all the

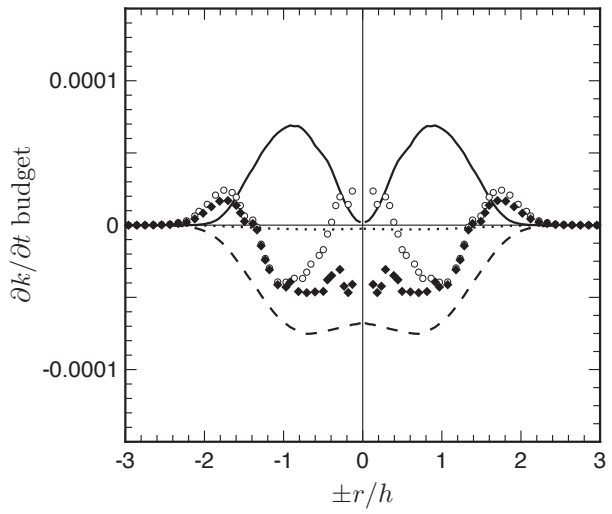

Figure 19. Radial profiles of terms in the TKE budget at $N\tilde{t} = 1.2$: ——, rate of production $\mathcal{P}_{\mathsf{tke}}$; – – – –, (minus) rate of dissipation $-\epsilon_{\mathsf{tke}}$; ·····, rate of buoyancy transfer $\mathcal{B}_{\mathsf{tke}}$; ∘, flux divergence $\mathcal{F}_{\mathsf{tke}}$; ♦, $\mathcal{P}_{\mathsf{tke}} - \epsilon_{\mathsf{tke}} + \mathcal{B}_{\mathsf{tke}} + \mathcal{F}_{\mathsf{tke}}$. Advection $-\overline{v}\partial k/\partial y - \overline{w}\partial k/\partial z$ is negligible compared to terms shown. Budget terms normalized by U_r^3/L_r, where reference velocity $U_r = 2.09U_{do}$ and reference length $L_r = h_o$.

fluxes, including the viscous ones, being included in $\mathcal{F}_{\mathsf{tke}}$ in figure 19, rather than only the inviscid, boundary-layer terms shown in [34].) But while the profile shapes of the budget terms for the Uberio & Freymuth experiment and the present simulation are comparable, their relative magnitudes are not – which provides further evidence for the non-universal nature of the turbulence for (unstratified) wakes generated by different objects [5,35],RCC.

The influence of the stratification upon the three dominant terms in the TKE budget, and in particular how they evolve in the y-z plane, can be observed in figure 20. To facilitate comparison, 'quadrant-averaged' contours of $\partial k/\partial t$, $\mathcal{P}_{\mathsf{tke}}$, $-\epsilon_k$ and $\mathcal{F}_{\mathsf{tke}}$ at selected times are combined in each plot, in the 'northwest', 'northeast', 'southwest' and 'southeast' quadrants, respectively. The lateral and vertical coordinates are scaled by their respective width or height, to clarify the spatial variations, and reveal the early 'kinematic' stratification effects, which act solely to flatten and widen the axisymmetric distributions. The black lines trace the shape and extent of the mean defect, via $0.05U_d$ and $0.5U_d$ contours, while the white-line contours indicated the dominant term(s) at each time.

At $N\tilde{t} = 2.5$ (figure 20*a*), the only indication of the beginning of the end of the 3D regime is the slight lack of axisymmetry in the flux term, which causes the net TKE growth at the edge of the wake to be larger at the sides than at the top and bottom. The production and dissipation are not yet deeply affected, since using the width and height to normalise the cross-plane axes causes them to maintain their (axisymmetric) radial shapes from the unstratified state (figure 19). The location of the maximum production is still just inside the $\overline{u} = 0.5U_d$ (i.e. $r = h$) contour (close to the location of the maximum TKE; see figure 8*b*), and the maximum dissipation falls between $r = h$ and the centerline. As is the case for the unstratified/axisymmetric state, the flux term plays a large role in setting the net $\partial k/\partial t$ variation, and is solely responsible for the TKE growth at the wake edge (since the dissipation tends to cancel the production here).

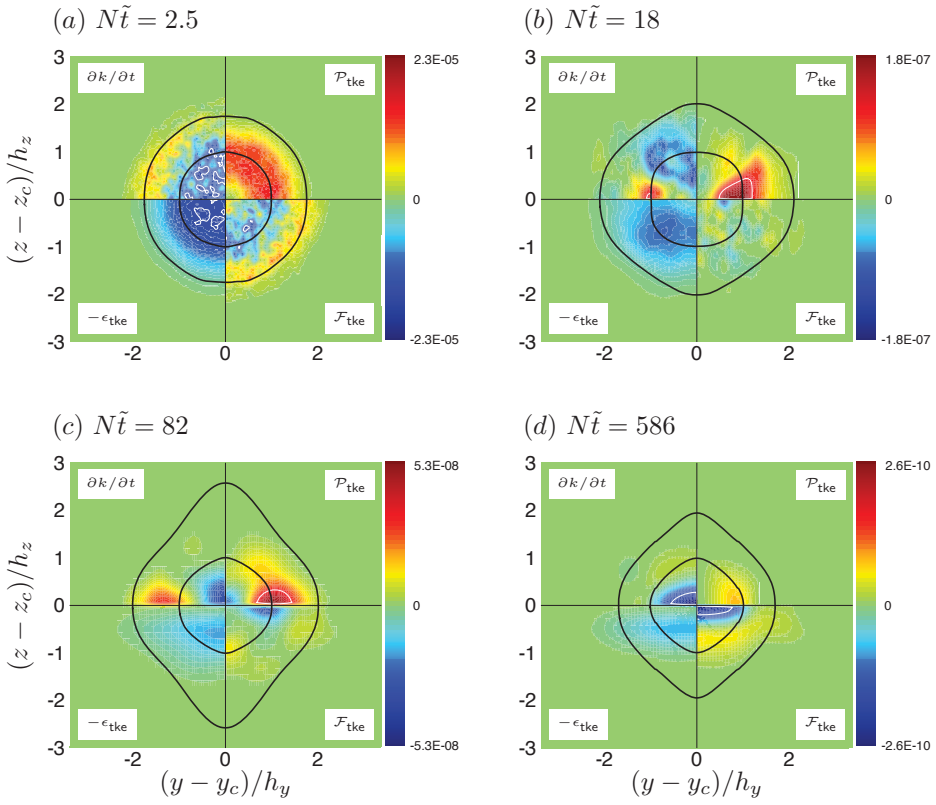

Figure 20. Contours of terms in TKE budget at: (*a*) $N\tilde{t} = 2.5$, (*b*) $N\tilde{t} = 18$, (*c*) $N\tilde{t} = 82$ and (*d*) $N\tilde{t} = 586$. Streamwise-averaged quantities have been further averaged ('double folded') across the lateral y and vertical z axes through the wake centerline (y_c, z_c), and plotted in separate quadrants, such that the upper left ('northwest'), upper right ('northeast'), lower left ('southwest') and lower right ('southeast') region of each plot respectively corresponds to the net rate of change $\partial k/\partial t = \mathcal{A}_{\mathsf{tke}} + \mathcal{P}_{\mathsf{tke}} + \mathcal{F}_{\mathsf{tke}} + \mathcal{B}_{\mathsf{tke}} - \epsilon_{\mathsf{tke}}$, production $\mathcal{P}_{\mathsf{tke}}$, (minus) dissipation $-\epsilon_{\mathsf{tke}}$ and flux-gradient transport $\mathcal{F}_{\mathsf{tke}}$. Buoyancy flux term $\mathcal{B}_{\mathsf{tke}}$ is shown in figure 17. Advection $\mathcal{A}_{\mathsf{tke}} = -\overline{v}\partial k/\partial y - \overline{w}\partial k/\partial z$ is negligible compared to the other terms. Budget terms normalized by U_r^3/L_r, where reference velocity $U_r = 2.09U_{do}$ and length $L_r = h_o$. White solid-line contours indicate ± 0.67 of the larger of the minimum and maximum magnitude at each time. Black solid-line contours correspond to $\overline{u} = 0.05U_d$ and $0.5U_d$. The (maximum,minimum) values at $N\tilde{t} = 2.5$, 18, 82 and 586 are respectively $(+1.49 \times 10^{-5}, -2.25 \times 10^{-5})$, $(+1.77 \times 10^{-7}, -1.1 \times 10^{-7})$, $(+5.3 \times 10^{-8}, -3.2 \times 10^{-8})$ and $(+8.15 \times 10^{-11}, -2.6 \times 10^{-10})$.

When the flow is well into the NEQ regime, $\mathcal{F}_{\mathsf{tke}}$ is much less significant, leaving the production-dissipation imbalance to control $\partial k/\partial t$ (figure 20*b*, for $N\tilde{t} = 18$). The dissipation has by this time become quite anisotropic, with $\epsilon_{\mathsf{tke}} \approx 2\tilde{\epsilon}_{11} \approx 4\tilde{\epsilon}_{22} \approx 5\tilde{\epsilon}_{33}$ (figure 16*b*). Nevertheless, its cross-plane variation – while tending to align into two flat regions above and below the y axis (consistent with the double-layer structure observed in figure 5, for $N\tilde{t} \approx 20$) – remains more axisymmetric than that of the production. In contrast, $\mathcal{P}_{\mathsf{tke}}$ tends to be concentrated into a 'wing-like' region near $y = \pm h_y$, because it is now nearly all associated with the $-\overline{u'v'}$ stress (Meunier *et al.* [3]), with $\mathcal{P}_{\mathsf{tke}} \approx P_{1122} = -\overline{u'v'}\partial\overline{u}/\partial y$. Consequently, the net $\partial k/\partial t \approx \mathcal{P}_{\mathsf{tke}} - \epsilon_{\mathsf{tke}}$ tends to be segregated according to sign, into either an 'hourglass'-shaped zone aligned with the z axis (TKE decay) or double 'hotspots' of TKE growth focused near $y = \pm h_y$. The latter is compatible with the 'double-pronged' structure in the TKE contours at $N\tilde{t} \approx 20$, seen in figure 8*c*.

The flow's entrance into its Q2D phase is characterized by the continuing importance of $\mathcal{P}_{\mathsf{tke}} \approx P_{1122}$, which is again concentrated along the y axis, near $y = \pm h_y$ (figure 20*c*, for $N\tilde{t} = 82$). However, the production now contains a small region of negative $\mathcal{P}_{\mathsf{tke}}$ centered at the origin, due to negative $P_{2222} = -\overline{v'v'}\partial\overline{v}/\partial y$. This is due to the combination of finite $\overline{v'v'}$ (whose maximum occurs at the centerline), and the positive $\partial\overline{v}/\partial y$ associated with the mean stagnation flow (i.e. vertical collapse and lateral expansion) at the origin. The dissipation is now even more concentrated in two flat regions above and below the y axis, within the $\overline{u} = 0.5U_d$ contour, than it was at $N\tilde{t} = 18$ – corresponding to the enhanced vertical shear mentioned by e.g. Spedding [12], and the primary roles played at this time by $\tilde{\epsilon}_{11} \sim \overline{(\partial u'/\partial z)^2}$ and $\tilde{\epsilon}_{22} \sim \overline{(\partial v'/\partial z)^2}$ (figure 16*b*). The flux-divergence term has grown in importance, compared to its $N\tilde{t} = 18$ levels, such that it significantly reduces $\mathcal{P}_{\mathsf{tke}}$ (near $y = \pm h_y$) and decreases ϵ_{tke} (near $z = \pm h_z$). The net result leads to the TKE distribution shown in figure 8*d*, which demonstrates the persistence of the flattened double-peaked structure as the flow passes from the NEQ to the Q2D regime (see also Brucker & Sarkar [9]).

Much later, at times for which the turbulence is dominated by the quasi-2D pancake eddies displayed in figure 6, the $\mathcal{P}_{\mathsf{tke}} \approx P_{1122}$ production is still active near $y = \pm h_y$, and ϵ_{tke} ($\approx 1.5\tilde{\epsilon}_{22}$) is still focused in horizontal layers near $z = \pm 0.5 h_z$, but both are weaker than the flux term $\mathcal{F}_{\mathsf{tke}}$. As is the case for $\mathcal{P}_{\mathsf{tke}}$ and ϵ_{tke}, the distribution of $\mathcal{F}_{\mathsf{tke}}$ is closely correlated with the two-layer pancake-eddy structure at this time. The largest (positive) vertical-gradient contribution $\partial f_3/\partial z$ is aligned with the horizontal layers centered near $z = \pm h_z/2$ (and thus reduces the effect of the dissipation here), while the smallest (negative) values lie between the layers, along the y axis; the maximum and minimum lateral divergence $\partial f_2/\partial y$ are clustered along the y axis, at the lateral edges of the dual $\mathcal{P}_{\mathsf{tke}}$ (and TKE) peaks, with the negative values closer to the wake centerline. The flux term combines with $\mathcal{P}_{\mathsf{tke}}$ and ϵ_{tke} to yield large negative $\partial k/\partial t$ in a shallow horizontal layer near the centerline. While there is still some TKE growth due to the combined effect of $\mathcal{P}_{\mathsf{tke}}$ and $\mathcal{F}_{\mathsf{tke}}$, between the y and z axes along the $\overline{u} = U_d$ contour, it is very weak.

3.6 Comparison with previous simulations

Figure 21 shows the mean-defect histories from earlier simulations at various Froude and Reynolds numbers, along with the present results ($F_{do} = 130$, $R_{do} = 2625$). Available DNS and a recent LES are included: The DNS of Gourlay *et al.* [13] ($F_{do} = 34$, $R_{do} = 1472$) and Brucker & Sarkar's [9] Case TR50F04 ($F_{do} \approx 0.75$, $R_{do} \approx 3250$) and TR10F20 ($F_{do} \approx 3.75$, $R_{do} \approx 650$), and Diamessis *et al.*'s [2] Case R100F64 LES ($F_{do} \approx 34$, nominal $R_{do} \approx 11,000$). Also shown are the unstratified/3D-regime power-law diagnostics for each case (inset plots in figure 21*a*, *b*). These are used to estimate virtual-time origins for each simulation, to facilitate comparison by plotting histories in terms of $N\tilde{t} = Nt - Nt_{vo}$.

The various histories cannot be expected to agree in the scaling used for figure 21, which

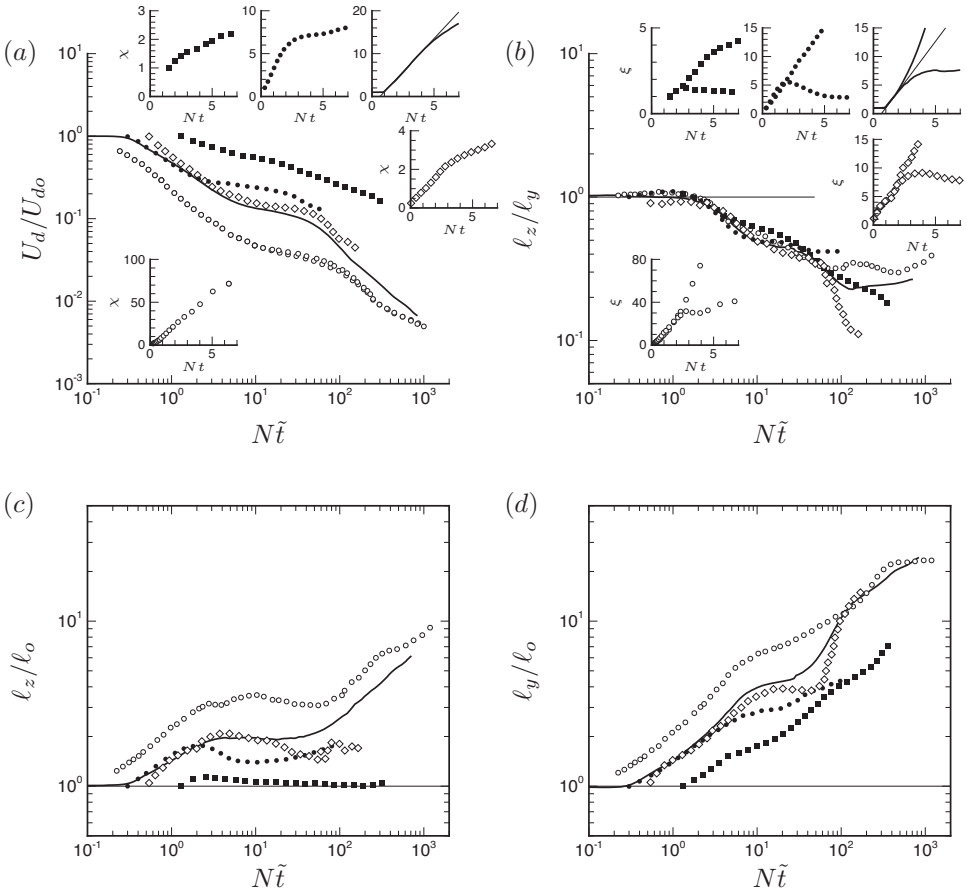

Figure 21. Histories of (a) maximum velocity U_d, (b) height-to-width ratio ℓ_z/ℓ_y, (c) height ℓ_z and (d) width ℓ_y of mean defect: ———, present; ○, [13]; ■, Case TR50F04 of [9]; •, Case TR10F20 of [9]; ◇, Case R100F64 LES of [2] . Inset plots in (a) and (b) show unstratified similarity diagnostics for (a) velocity $\chi = (U_d/U_{do})^{-3/2}$ and (b) height $\xi_z = (\ell_z/\ell_o)^3$ (lower curve/symbols) and width $\xi_y = (\ell_y/\ell_o)^3$ (upper curve/symbols), which are used to define the virtual-time origin t_{vo} for each case, with $Nt_{vo} = 0.645$ for the present DNS, $Nt_{vo} = 0.2$ for Brucker & Sarkar's TR50F04, $Nt_{vo} = -0.5$ for Diamessis *et al.* and $Nt_{vo} = 0$ for Gourlay *et al.* [13] and Brucker & Sarkar's [9] TR10F20. For the present DNS, the linear curve-fit for χ and ξ (——— in upper right-hand-side inset plots in a and b) are $\chi = (U_d/U_{do})^{-3/2} = B \cdot N\tilde{t}$ and $\xi = (r^*/r_o^*)^3 = C \cdot N\tilde{t}$, where $N\tilde{t} = Nt - Nt_{vo}$ and $(B, C, Nt_{vo}) = (3.1, 2.9, 0.645)$. The maximum defect velocity U_d in (a) for Brucker & Sarkar's [9] Case TR50F04 (but not TR10F20) is replaced by their $U_1^{m.k.e.}$. Integral measures are used for the height and width for the present DNS, with $\ell_z = r_z^*$, $\ell_y = r_y^*$, and ℓ_o the value of $r_z^* = r_y^*$ at $Nt = 0$. For Brucker & Sarkar's [9] Case TR50F04, ℓ_z and ℓ_y are respectively represented by integral scales (in their notation) R_3 and R_2, with ℓ_o the half-radius of the initial Gaussain mean-velocity profile, while for Diamessis *et al.* [2], and effectively for Gourlay *et al.* [13], $\ell_z = h_z$, $\ell_y = h_y$ and $\ell_o = h_o$, where h_z and h_y are determined from fitting an assumed Gaussian profile.

takes no account of Froude and/or Reynolds numbers, since the maximum velocities U_d, heights ℓ_z, and widths ℓ_y are presented solely in terms of their initial values. (Also, ℓ_z is for some cases given in terms of the $0.5U_d$ half-height h_z and for others in terms of integral measures; see figure 21*c* caption.) Nevertheless, several common features can be observed, including similar power-law behavior over the same $N\tilde{t}$ range. The height decreases with time for $N\tilde{t} > 2$ in every case, although the reduction of h_z is larger than that experienced by the integral-measure heights (which is consistent with the behavior found for the present DNS, in that both $\mathrm{d}h_z/\mathrm{d}t$ and $\mathrm{d}r_z^*/\mathrm{d}t$ are negative for $8 < N\tilde{t} < 18$, but h_z falls faster than r_z^*; figure 7*b*).

The 3D-to-NEQ transition also tends to occur at about the same time for each of the simulations, with $N\tilde{t}$ between 2 to 2.5 the point at which the the heights and widths first begin to differ from each other; this can be seen in figure 21*b*, in both the height-to-width ratio ℓ_z/ℓ_y and is even more obvious in the unstratified/axisymmetric height/width diagnostic $\xi = (\ell/\ell_o)^3$ shown in the inset plots (recall that linear variation with time of ξ is characteristic of the pure-axisymmetric 3D regime).

The reasonably good collapse of the mean aspect ratio ℓ_z/ℓ_y over the early NEQ periods of the five simulations was not anticipated, both because of the wide Froude and Reynolds number ranges, as well as the differences in the initialization strategies used for the various simulations (e.g. Brucker & Sarkar's [9] DNS held the mean velocity fixed until $Nt = 0.2$ (TR10F20) and 1 (TR50F04), while Diamessis *et al.*'s [2] LES gradually introduced the background stratification during a precursor simulation). The ℓ_z/ℓ_y histories again demonstrate the increase of the $N\tilde{t}$ range of the NEQ regime with Reynolds number – compare the times at which the ℓ_z/ℓ_y histories begin to deviate from the negative power-law behavior for NEQ, for Brucker & Sarkar's [9] TR10F20 ($40 < N\tilde{t} < 100$), Gourlay *et al.* [13] ($N\tilde{t} \approx 70$), present ($N\tilde{t} \approx 105$), and Brucker & Sarkar's [9] TR50F04 ($N\tilde{t} > 400$, at least). (The late-time ℓ_z/ℓ_y history for Diamessis *et al.* [2] (open diamonds) is thought to be statistically unreliable, in light of the relatively small streamwise domain used.) The same message regarding the Reynolds-number dependence of the NEQ period can be inferred from figure 21*c*, by examining the durations of the $\mathrm{d}\ell_z/\mathrm{d}t \approx 0$ regions for each case.

The tendency for ℓ_z and ℓ_y to deviate from the 3D/axisymmetric ideal sooner than U_d does, which was seen above (figure 7), also holds for the other simulations (although not as markedly), since the unstratified/axisymmetric similarity diagnostic for U_d, $\chi = (U_d/U_{do})^{-3/2}$, remains linear longer (until $N\tilde{t} \approx 2$ to 2.5) than the corresponding height/width diagnostic, ξ ($N\tilde{t} \approx 2$ to 5); cf. figures 21*a* and *b* inset plots.

A scaling to account for the significant Froude-number sensitivity of the U_d histories seen in figure 21*a* has been developed by Meunier & Spedding [17]. It amounts to assuming U_d will eventually depend solely on the volume-flux deficit I_d, the Brunt-Väisälä frequency N and time t, which leads via dimensional analysis to

$$\frac{U_d}{(I_d N^2)^{1/3}} = \Phi(Nt - Nt_0), \tag{8}$$

where Φ is a universal non-dimensional function of $Nt - Nt_0$ and Nt_0 is a non-universal offset time (unrelated to the 3D virtual-origin time Nt_{vo}), which will depend for example on Reynolds number and the near-field/early-time wake evolution. In terms of a virtual wake-creating sphere of diameter D emersed in a steady uniform stream of density ρ_∞ and speed V_∞, experiencing a drag force F_D, we can write $I_d = \frac{1}{8} V_\infty D^2 C_D$, where $C_D = F_D/(\pi \rho_\infty V_\infty^2 D^2/8)$. Equation (8) then implies

$$\frac{U_d}{V_\infty} F_\infty^{2/3} = f(C_D)\Phi(Nt - Nt_0), \tag{9}$$

where $f(C_D) = (\pi C_D/2)^{1/3}$. Equation (9) shows the limitation of attempting to collapse U_d/V_∞ data from wakes generated by various bluff bodies (with variable C_D) by using only

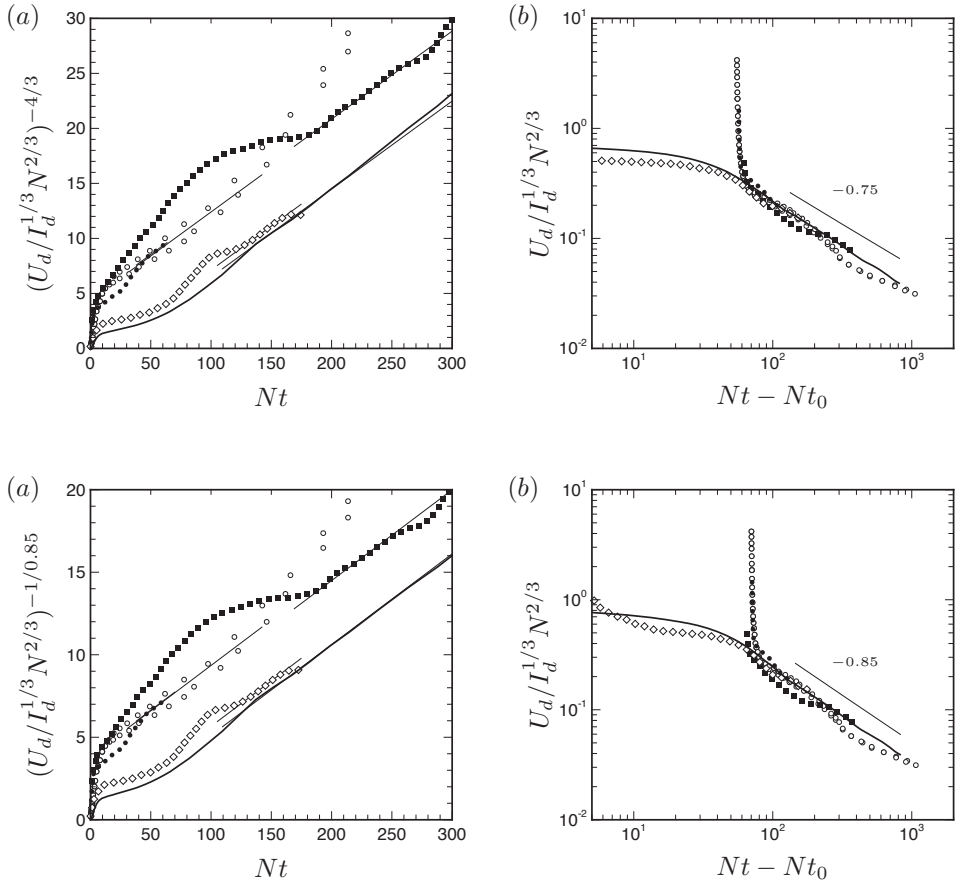

Figure 22. Histories of rescaled mean defect (a, c) as Q2D power-law/similarity diagnostic and (b, d) with respect to Q2D time shift Nt_0, assuming (a, b) $n = 3/4$ and (c, d) $n = 0.85$: ———, present DNS; ○, Gourlay *et al.* [13]; ■, Case TR50F04 of Brucker & Sarkar [9]; •, Case TR10F20 of [9]; ⋄, Case R100F64 LES of Diamessis *et al.* [2]. Thin-solid curves (———) in (a, c) are linear curve fits of Q2D diagnostic (which for [13] and Case TR10F20 of [9] are nearly coincident), used to define time shift Nt_0 in (b, d), such that for (b) $(n = 3/4)$ $Nt_0 =: 19$ (present DNS), -55 ([13]), -63.5 (Case TR50F04 of [9]), -57 (Case TR10F20 of [9]) & 11 (Case R100F64 of [2]), and for (b) $(n = 3/4)$ $Nt_0 =: 7$ (present DNS), -70 ([13]), -66.5 (Case TR50F04 of [9]), -71 (Case TR10F20 of [9]) & -3 (Case R100F64 of [2]).

F_∞ (e.g. by plotting $(U_d/V_\infty)F_\infty^{2/3}$ versus Nt; cf. [1,9]). Following Meunier & Spedding [17], (8) can be recast in terms of the virtual effective diameter $D_{\rm eff} = D(C_D/2)^{1/2}$ for bluff bodies of arbitrary shape,

$$\frac{U_d}{V_\infty}\mathrm{F}_{\rm eff}^{2/3} = \pi^{1/3}\Phi(Nt - Nt_0), \tag{10}$$

where $\mathrm{F}_{\rm eff} = 2V_\infty/ND_{\rm eff}$ is the effective Froude number.

The validity of (8) is tested in figure 22. Meunier & Spedding [17] found the universality under consideration cannot be expected until the flow reaches the Q2D regime (see their figure 5*b*). Consequently, we assume $\Phi(Nt - Nt_0) = C_{Q2D}(Nt - Nt_0)^{-n}$, where C_{Q2D} is a universal constant and $n \approx 3/4$. Similar slopes of the $(U_d/I_d^{1/3}N^{2/3})^{-1/n}$ diagnostic are found for all five simulations, for both $n = 3/4$ (figure 22*a*, with $C_{Q2D} = 0.08^{-3/4} \approx 6.65$) and the $n = 0.85$ suggested by the present DNS (figure 22*c*; $C_{Q2D} = 0.055^{-0.85} \approx 11.8$). Note the dependence of the beginning of the region of common slope (straight thin-solid lines in figure 22*a*, *c*), and the offset times Nt_0 (Nt-axis intercept), on the Reynolds number and initialization scheme used by each simulation. The reasonable collapse of the results in figures 22*b* and *d*, produced by using the Nt_0 defined for each case by the corresponding curve fits in figures 22*a* and *c*, points to the validity of (8), and thus to that of the founding assumptions used in the Meunier & Spedding [17] analysis.

4 Summary and closing comments

The DNS results presented above reveal the effect of a weakly stratified, buoyantly stable background upon the structure and statistics of a turbulent wake, during its various phases of development, including its 3D, NEQ and Q2D regimes. This has been documented by the evolution of the mean momentum and energy, turbulence kinetic energy, and the terms in their budgets. The dependence of the quality of the statistics on adequate 'eddy sample size' has been observed, as has the Reynolds-number dependence of the duration, in terms of Nt, of the NEQ regime.

The mean momentum budget clarifies the relationship between the turbulence suppression due to buoyancy and the turbulent and viscous mechanisms responsible for the vertical and lateral growth of the wake. The TKE budget, on the other hand, quantifies the manner in which the changes in turbulence structure are reflected in changes to the relative importance and composition of the terms whose imbalance defines the net rate of change of TKE. Surprisingly, despite these changes in structure, the TKE dissipation decays at approximately the same rate during the early/3D and late/Q2D regimes. This affirms yet again the dissimilarity between the Q2D state and pure 2D turbulence [11].

The present results illustrate that the wake collapse, signaling the beginning of the NEQ regime, need not be accompanied by the transfer from the potential energy of the turbulence to the kinetic energy of the turbulence, as has been proposed elsewhere. Instead, the enhanced TKE exhibited during the NEQ regime is solely the result of buoyancy-induced structural changes, which lead to increased TKE production. Thus, while the potential-to-kinetic energy transfer is observed at early times for lower F_∞ cases (Dommermuth *et al.* [8]; Brucker & Sarkar [9]), it is not an essential feature of the 3D to NEQ transition.

For the present high-F_∞ case, internal wave activity is most pronounced at the start of the NEQ regime. However, even during this time, internal waves make a negligible contribution to the turbulence energy budget. This is in contrast to the strongly stratified cases studied elsewhere, for which the amount of turbulence energy radiated by internal waves during the NEQ regime can be comparable to that produced by the mean shear or lost via viscous dissipation (cf. Brucker & Sarkar [9]).

The role of stable stratification in driving the wake towards a universal state has also been displayed, in that the Q2D structure is independent of the details of the wake initializa-

tion (a fact frequently observed in other experiments and simulations). The present study also indicates that during the Q2D period, the history of the maximum mean defect U_d (appropriately normalized, in terms of the initial volume-flux deficit I_d and the Brunt-Väisälä frequency N) is a unique function of nondimensional time Nt (relative to a flow-dependent virtual offset/origin). This supports the validity of the framework proposed by Meunier & Spedding [17] in their universal model of the mean-defect evolution for a stably stratified towed wake.

References

1. Spedding, G. R.: The evolution of initially turbulent bluff-body wakes at high internal Froude number. *J. Fluid Mech.*, vol. 337, 1997, pp. 283–301.

2. Diamessis, P. J.; Spedding, G. R.; and Domaradzki, J. A.: Similarity scaling and vorticity structure in high-Reynolds-number stably stratified turbulent wakes. *J. Fluid Mech.*, vol. 671, 2011, pp. 52–95.

3. Meunier, P.; Diamessis, P. J.; and Spedding, G. R.: Self-preservation in stratified momentum wakes. *Phys. Fluids*, vol. 18, 2006, p. 106601.

4. Tennekes, H.; and Lumley, J.: *A First Course in Turbulence*. The MIT Press, 1972.

5. Bevilaqua, P. M.; and Lykoudis, P. S.: Turbulence memory in self-preserving wakes. *J. Fluid Mech.*, vol. 89, no. 3, 1978, pp. 589–606.

6. Chomaz, J. M.; Bonneton, P.; Butet, A.; and Hopfinger, E. J.: Vertical diffusion of the far wake of a sphere moving in a stratified fluid. *Phys. Fluids*, vol. 5, no. 11, 1993, pp. 2799–2806.

7. Riley, J. J.; and Lelong, M.-P.: Fluid motions in the presence of strong stratification. *Annu. Rev. Fluid Mech.*, vol. 32, 2000, pp. 613–657.

8. Dommermuth, D. G.; Rottman, J. W.; Innis, G. E.; and Novikov, E. A.: Numerical simulation of the wake of a towed sphere in a weakly stratified fluid. *J. Fluid Mech.*, vol. 473, 2002, pp. 83–101.

9. Brucker, K. A.; and Sarkar, S.: A comparative study of self-propelled and towed wakes in a stratified fluid. *J. Fluid Mech.*, vol. 652, 2010, pp. 373–404.

10. Lin, J. T.; and Pao, Y. H.: Wakes in stratified fluids. *Ann. Rev. Fluid Mech.*, vol. 11, 1979, pp. 317–338.

11. Godeford, F. S.; and Cambon, C.: Detailed investigation of energy transfer in homogeneous stratified turbulence. *Phys. Fluids*, vol. 6, no. 6, 1994, pp. 2084–2100.

12. Spedding, G. R.: Vertical structure in stratified wakes with high initial Froude number. *J. Fluid Mech.*, vol. 454, 2002, pp. 71–112.

13. Gourlay, M. J.; Arendt, S. C.; Fritts, D. C.; and Werne, J.: Numerical modeling of initially turbulent wakes with net momentum. *Phys. Fluids*, vol. 13, no. 12, 2001, pp. 3783–3802.

14. Redford, J. A.; Castro, I. P.; and Coleman, G. N.: On the universality of turbulent axisymmetric wakes. *J. Fluid Mech.*, vol. 710, 2012, pp. 419–452 (referred to herein as RCC).

15. Bonnier, M.; Bonneton, P.; and Eiff, O.: Far-wake of a sphere in a stably stratified fluid. *Appl. Sci. Res.*, vol. 59, 1998, pp. 269–281.

16. Pal, A.; de Stadler, M. B.; and Sarkar, S.: The spatial evolution of fluctuations in a self-propelled wake compared to a patch of turbulence. *Phys. Fluids*, vol. 25, 2013, p. 095106.

17. Meunier, P.; and Spedding, G. R.: A loss of memory in stratified momentum wakes. *Phys. Fluids*, vol. 16, 2004, pp. 298–305.

18. de Stadler, M. B.; and Sarkar, S.: Simulation of a propelled wake with moderate excess momentum in a stratified fluid. *J. Fluid Mech.*, vol. 692, 2012, pp. 28–52.

19. de Stadler, M. B.; Sarkar, S.; and Brucker, K. A.: Effect of Prandtl number on a stratified turbulent wake. *Phys. Fluids*, vol. 22, 2010, p. doi:10.1063/1.3478841.

20. Gottlieb, D.; and Orszag, S. A.: *Numerical analysis of spectral methods: theory and applications*. SIAM, 1977.

21. Kim, J.; Moin, P.; and Moser, R.: Turbulence statistics in fully developed channel flow at low Reynolds number. *J. Fluid Mech.*, vol. 177, 1987, pp. 133–166.

22. Spalart, P. E.; Moser, R. D.; and Rogers, M. M.: Spectral methods for the Navier–Stokes equations with one infinite and two periodic directions. *J. Comput. Phys.*, vol. 96, no. 2, 1991, pp. 297–324.

23. Rogallo, R. S.: Numerical experiments in homogeneous turbulence. NASA Technical Memorandum 81315, 1981.

24. Shariff, K.; Verzicco, R.; and Orlandi, P.: Three-dimensional vortex ring instabilities. *J. Fluid Mech.*, vol. 279, 1994, pp. 351–375.

25. Spedding, G. R.; Browand, F. K.; and Fincham, A. M.: Turbulence, similarity scaling and vortex geometry in the wake of a towed sphere in a stably stratified fluid. *J. Fluid Mech.*, vol. 314, 1996, pp. 53–103.

26. Redford, J. A.; Llor, A.; and Watteaux, R.: Self-similarity of variable acceleration Rayleigh-Taylor turbulent mixing layers. *Proceedings of the ETMM9 Engineering Turbulence Measurement and Modelling symposium, ETMM9, Thessaloniki, Greece, June 6–8, 2012.*, 2012.

27. Mowbray, D. E.; and Rarity, B. S. H.: A theoretical and experimental investigation of the phase configuration of internal waves of small amplitude in a density stratified liquid. *J. Fluid Mech.*, vol. 28, 1967, pp. 1–16.

28. Turner, J. S.: *Buoyancy Effects in Fluids*. Cambridge University Press, 1973.

29. Lighthill, M. J.: *Waves in Fluids*. Cambridge University Press, 1978.

30. Spedding, G. R.: Anisotropy in turbulence profiles of stratified wakes. *Phys. Fluids*, vol. 13, 2001, pp. 2361–2372.

31. Townsend, A.: *The Structure of Turbulent Shear Flow*. Cambridge University Press, 2 ed., 1976.

32. Itsweire, E. C.; Koseff, J. R.; Brigss, D. A.; and Ferziger, J. H.: Turbulence in stratified shear flows: implications for interpreting shear-induced mixing in the ocean. *J. Phys. Oceanogr.*, vol. 23, 1993, pp. 1508–1522.

33. Bradshaw, P.: Effects of extra rates of strain – review. *Zoran Zaric Mem. Seminar, Dubrovnik.* Hemisphere, 1988.

34. Uberoi, M. S.; and Freymuth, P.: Turbulent energy balance and spectra of the axisymmetric wake. *Phys. Fluids*, vol. 13, no. 9, 1970, pp. 2205–2210.

35. Johansson, P. B. V.; George, W. K.; and Gourlay, M. J.: Equilibrium similarity, effects of initial conditions and local Reynolds number on the axisymmetric wake. *Phys. Fluids*, vol. 15, no. 3, 2003, pp. 603–617.

REPORT DOCUMENTATION PAGE

Form Approved
OMB No. 0704-0188

1. REPORT DATE *(DD-MM-YYYY)*	2. REPORT TYPE	3. DATES COVERED *(From - To)*
01- 09 - 2014	Technical Memorandum	

4. TITLE AND SUBTITLE

Direct Numerical Simulation of a Weakly Stratified Turbulent Wake

5a. CONTRACT NUMBER

5b. GRANT NUMBER

5c. PROGRAM ELEMENT NUMBER

6. AUTHOR(S)

Redford, J. A.; Lund, T. S.; Coleman, Gary N.

5d. PROJECT NUMBER

5e. TASK NUMBER

5f. WORK UNIT NUMBER

794072.02.07.02.03

7. PERFORMING ORGANIZATION NAME(S) AND ADDRESS(ES)

NASA Langley Research Center
Hampton, VA 23681-2199

8. PERFORMING ORGANIZATION REPORT NUMBER

L-20448

9. SPONSORING/MONITORING AGENCY NAME(S) AND ADDRESS(ES)

National Aeronautics and Space Administration
Washington, DC 20546-0001

10. SPONSOR/MONITOR'S ACRONYM(S)

NASA

11. SPONSOR/MONITOR'S REPORT NUMBER(S)

NASA/TM-2014-218523

12. DISTRIBUTION/AVAILABILITY STATEMENT

Unclassified - Unlimited
Subject Category 01
Availability: NASA CASI (443) 757-5802

13. SUPPLEMENTARY NOTES

14. ABSTRACT

Direct numerical simulation (DNS) is used to investigate a time-dependent turbulent wake evolving in a stably stratified background. A large initial Froude number is chosen to allow the wake to become fully turbulent and axisymmetric before stratification affects the spreading rate of the mean defect. The uncertainty introduced by the finite sample size associated with gathering statistics from a simulation of a time-dependent flow is reduced, compared to earlier simulations of this flow. The DNS reveals the buoyancy-induced changes to the turbulence structure, as well as to the mean-defect history and the terms in the mean-momentum and turbulence-kinetic-energy budgets, that characterize the various states of this flow -namely the three-dimensional (essentially unstratified), non-equilibrium (or 'wake-collapse') and quasi-two-dimensional (or 'two-component') regimes observed elsewhere for wakes embedded in both weakly and strongly stratified backgrounds. The wake-collapse regime is not accompanied by transfer (or 'reconversion') of the potential energy of the turbulence to the kinetic energy of the turbulence, implying that this is not an essential feature of stratified-wake dynamics. The dependence upon Reynolds number of the duration of the wake-collapse period is demonstrated, and the effect of the details of the initial/near-field conditions of the wake on its subsequent development is examined.

15. SUBJECT TERMS

Direct numerical simulation; Stratification; Turbulence; Turbulent wakes; Wakes

16. SECURITY CLASSIFICATION OF:			17. LIMITATION OF ABSTRACT	18. NUMBER OF PAGES	19a. NAME OF RESPONSIBLE PERSON
a. REPORT	b. ABSTRACT	c. THIS PAGE			STI Help Desk (email: help@sti.nasa.gov)
					19b. TELEPHONE NUMBER *(Include area code)*
U	U	U	UU	49	(443) 757-5802